EUROPEAN JOURNAL OF PURE AND APPLIED MATHEMATICS
2025, Vol. 18, Issue 4, Article Number 6903
ISSN 1307-5543 – ejpam.com
Published by New York Business Global

Time-Fractional Free Convection of Maxwell, Williamson, and Micropolar Nanofluids over a Vertical Plate in Saturated Porous Media

Hossam A. Nabwey[1,*], M. M. Nour[1], Assma S Zaki[2], Waqar A. Khan[3], A. M. Rashad[2], Amal M. A. EL-Hakiem[2], Abdallah Alderayhim[1], Mohamed M. Awad[1]

[1] *Department of Mathematics, College of Science and Humanities in Al-Kharj, Prince Sattam bin Abdulaziz University, Al-Kharj 11942, Saudi Arabia*
[2] *Department of Mathematics, Aswan University, Faculty of Science, Aswan, 81528, Egypt*
[3] *Department of Pure and Applied Mathematics, Saveetha School of Engineering, Saveetha Nagar, Thandalam, Chennai-602105, Tamil Nadu, India*

Abstract. This study develops a unified time-fractional framework to investigate free convection of Maxwell, Williamson, and micropolar nanofluids in porous media under the combined effects of magnetic field, thermal radiation, and internal heat generation. The governing fractional-order equations are transformed using similarity variables and solved numerically with Maple 24. Unlike earlier studies that treated individual models, the present work simultaneously incorporates elasticity, shear-thinning, and microrotation mechanisms, enabling direct comparisons of heat and mass transfer characteristics across these non-Newtonian nanofluids. Results show that Williamson nanofluids outperform Maxwell and micropolar fluids, yielding Nusselt numbers up to $18-22\%$ higher and Sherwood numbers up to $15-20\%$ higher due to their shear-thinning behavior. Internal heat generation is found to increase fluid motion by approximately 12% in terms of velocity magnitude. Still, it reduces surface heat transfer rates by about $10-14\%$, reflecting a trade-off between buoyancy enhancement and thermal resistance. The influence of fractional order is significant: reducing the order from $\alpha = 1.0$ to $\alpha = 0.7$ decreases wall heat flux by nearly 17%, confirming the memory-dependent damping effect of fractional dynamics. These quantitative insights guide the selection and optimization of non-Newtonian nanofluids in applications such as magnetic refrigeration, porous heat exchangers, and advanced thermal energy systems.

2020 Mathematics Subject Classifications: 76S05, 76W05, 74S40, 76R10
Key Words and Phrases: Fractional numerical analysis, heat and mass transport, micropolar nanofluid, Maxwell and Williamson nanofluids, porous media, magnetic field, internal heat generation, thermal radiation

*Corresponding author.
DOI: https://doi.org/10.29020/nybg.ejpam.v18i4.6903

Email addresses: eng$_h$*ossam*21@*yahoo.com* (*H.A.Nabwey*), m.mohamednour@psau.edu.sa (M. M. Nour), zasmaasabry@yahoo.com (A. S. Zaki), wkhan1956@gmail.com (W. A. Khan), am$_r$*ashad*@*yahoo.com* (*A.M.Rashad*), elhakiem.amal@gmail.com (A. M. A. El-Hakiem), amaldurayhim@psau.edu.sa (A. Alderayhim), m.abdelgalil@psau.edu.sa (M. M. Awad)

1. Introduction

One of the most fascinating research topics of the past 200 years is the phenomenon of natural convection in porous media. Its widespread use in various industries, including metallurgy, nuclear power, filtration processes, thermal insulation, oceanography, geothermal systems, building insulation, geophysics, cooling of electronic devices, and separation processes in the chemical industry, is the reason for this interest. The monographs by Nield and Bejan [1], Ingham and Pop [2], and Vafai [3] provide excellent assessments of these applications, the governing equations, and the various phases of this area. Through a truncated cone in porous media, Rashad and Chamkha [4] demonstrated natural convection flow influenced by radiation and chemical processes. Jan et al. [5] investigated how wall slide affected the free convection flow through an infinite orthogonal plate with mass and heat transport.

The technological sector places great importance on the magnetohydrodynamic (MHD) natural heat flux due to its applications in geothermal and manufacturing technologies, liquid metal fluids, and hydromagnetic energy-generating systems. Due to its applications in industry and technology, numerous researchers have investigated spontaneous convective flow in the presence of magnetic fields. Chamkha [6] investigated the mass and heat transfer of free convective boundary layer flow via an isothermal truncated cone in a magnetic field. Rapits and Singh conducted a numerical analysis of the free convective flow through an accelerating orthogonal plate [7]. Palani and Kim [8] conducted a numerical study of the natural convective flow through an orthogonal cone exposed to a surface with a changing temperature in the presence of radiation and a magnetic field. References ([9–12]) provide studies that examine the heat and fluid flow properties along various geometries in a porous medium under the influence of a magnetic field. The impact of the sinusoidal surface temperature on the free convective flow of an MHD nanofluid down a vertical plate was examined by El-Zahar et al. [13]. The unstable slip flow of an MHD nanofluid across a radiative stretchable surface with convective heating was examined by Nabwey et al. [14].

The two main types of fluid dynamics are Newtonian and non-Newtonian fluids. Newtonian's viscosity law stipulates that viscosity should remain constant regardless of stress, and is not followed by a Non-Newtonian fluid. When non-Newtonian fluids are subjected to a force, their viscosity can change, becoming either more liquid or solid. Ketchup is a non-Newtonian fluid, as evidenced by its tendency to become runnier with shaking. Many researchers have extensively explored non-Newtonian fluids due to their use in various industrial operations. Products created with these fluids include filters, optical fibers, permeable pipelines, coated sheets, and polymeric polymers. Williamson [15] explained the flow of pseudoplastic materials. He also proposed a model equation for the flow of pseudoplastic fluid, the results of which were validated experimentally. Mahmood et al. [16] studied a mixed convective unstable stagnation point flow of Casson fluid caused by a vertical Riga surface. Paulo [17] provided an alternative rationale for applying characteristic values in non-dimensionalizing the governing equations of non-Newtonian fluid flow problems. The computational analysis of thermal transport in Williamson fluid flow

with heat generation or absorption over an expanding cylinder was studied by Malik et al. [18]. Sharada and Shankar examined the Joule heating of a Williamson fluid in an MHD mixed convective flow with slip over an exponentially extending surface [19]. Algehyne et al. [20] studied a Casson and Oldroyd-B fluid flowing in a combined convective flow over a layered stretched sheet with nonlinear thermic radiation and chemical reaction. The Jeffrey fluid model, which offers a more accurate description than traditional viscous models, is employed by Khan et al. [21] to investigate stress relaxation in non-Newtonian fluids.

The development of compact thermal devices has led to a growing concern in the modern world for enhancing heat transfer. Applying both active and passive methods can enhance heat convection in many thermal devices. Active techniques utilize mechanical tools, including electric or magnetic fields, suction, injection, and radiative heat, to enhance heat transfer. On the other hand, passive operations include changing domains, improving surfaces, and using fluid nanofluids. The components of nanofluids are nanoparticles with a size range of less than 1-100 nm and liquids with low heat conductivity, such as water, kerosene oil, and ethylene glycol. Due to their morphological, structural, and compositional properties, nanoparticles are suitable for various real-world applications, including nuclear reactors, power plants, solar panels, oil extraction, and fermentation. Choi and Eastman [22] investigated the fundamental concept of nanofluids in 1995 to enhance the thermodynamic properties of ordinary fluids. According to research by Kumar et al. [23], Gireesha et al. [24], Saleem et al. [25], Weng et al. [26], Islam et al. [27], Rafique et al. [28], Anwar et al. [29], and Khan et al. [30], nanofluids have been extensively published and have gained significance as a material to construct highly efficient thermic devices in recent years. Rafique et al. [31] provided a detailed study of double-diffusive Casson nanofluid flow over a solid sphere at lower stagnation point flow in the presence of quadratic thermal radiation, heat generation, and magnetic field effects. Nadhish et al. [32] investigated the impacts of heat transfer, mass transfer, and entropy generation optimization on a ternary hybrid nanofluid moving down an inclined channel in the presence of an induced magnetic field. Nabwey et al. [33] explained non-Newtonian Carreau ternary hybrid nanofluid flow with heat transfer via an exponentially extending curved surface. Examining how heat stratification affects the MHD flow of water-based nano, hybrid, and ternary hybrid nanofluids as they traverse a vertically extending cylinder in a porous medium is studied by Nath and Deka [34].

Theories of fluid flow that account for the nanoparticles' microrotation may be able to explain both the experimental and theoretical data. Micropolar fluid theory is the term used to describe this concept. One could think of Eringen's [35] introduction of microplastic fluids as a generalization of the Navier-Stokes equations. Since they consider the fluid's microstructure and the inertial properties of the substructure particles permitted to rotate, they are a subclass of microfluids. A simple microfluid is a fluid medium whose behavior and attributes are greatly impacted by the local motions of the material particles contained in each of its volume elements, according to Eringen's concept of microfluids. In other words, a microfluid is a viscous isotropic fluid with local inertia of motion. From a physical perspective, the rotation of particles is described by a new kinematic variable, mi-

crorotation, introduced by this model. The effects of particle microrotations can be more easily explained when microfluids are broken down into smaller classes due to their intricate formulation. Rigid particles trapped in a small volume element can spin about their center, which is defined by the microrotation vector [36, 37]. This rotation is independent of the mean fluid flow and its local vorticity field, and is particularly evident in micropolar fluids, a subclass of microfluids. An analogous solution for the free convective flow of a micropolar nanofluid through an orthogonal plate in a saturated porous medium, influenced by a magnetic field, is presented by Mansour et al. [38]. Arya et al. [39] examined the effects of viscous dissipation and magnetohydrodynamics on micropolar fluid thermal stratification over a a curved stretched sheet. Kumar et al. [40] investigated the heat and mass transport properties of a micropolar nanofluid flowing across a linearly stretching and contracting porous surface. The flow was an incompressible, constant, two-dimensional laminar MHD boundary layer. Khan et al. [41] investigated the properties of a micropolar nanofluid containing microorganisms in relation to temperature and flow. A crucial concept in the study of fluid dynamics is the Darcy-Forchheimer relation, which is used to understand the pressure decrease a fluid experiences when passing through a porous material or a conduit with increased resistance. Using the Buongiorno nanofluid model, the heat and mass transport properties of micropolar Maxwell and Williamson nanofluids passing by a perpendicular cylinder under the impact of coupled convective flow are examined by Nabwey et al. [42]. The behavior of magneto-Williamson and Maxwell micropolar nanofluid flow across a non-isothermal wedge is explained by Khan et al. [43].

Finally, fractional calculus plays an essential role in most fields of life (see references [44–48]. Consequently, many scientists focus on studying mathematical models using various methods involving fractional derivatives. The concept was initially brought to the literature by Gottfried Wilhelm Leibniz [49] and then developed by Niels Henrik Abel [50], Riemann-Liouville, Riesz, Caputo (see [51]), Hadamard [52], and Atangana-Baleanu [53]. Fractional calculus deals with nonlocal integration and differentiation [54]. Raza et al. [55] discussed an unstable, viscous, and incompressible hybrid Brinkmann nanofluid composed of graphene oxide and molybdenum disulfide, suspended in water, with carboxymethyl cellulose as the base fluid. Ming Shen et al. [56] provided an overview of current advances in nanofluid models using fractional derivatives. The improved thermal conductivity of single and hybrid nanofluids opens up numerous practical and potential uses. Existing theories are unable to explain the abnormal thermal behavior of these fluids. Asjad et al. [57] employed a fractional system to investigate the impact of generalized boundary conditions on the thermal conductivity properties of nanofluids. Ikram et al. [58] developed various fractional models to investigate the heat transfer efficiency of hybrid nanofluids during channel flows. Khan et al. [59] demonstrated the improved convective heat transfer of nanofluids containing gamma alumina nanoparticles in water and EG bases, emphasizing the impact of the effective Prandtl number in thermal and flow dynamics, using a unique double-fractional constitutive model and experimentally determined models for viscosity and thermal conductivity. The mixed convection flow of fractional nanofluids over a stretching surface, considering the effect of the Prandtl number, is investigated by Khan et al. [60]. Khan et al. [61] studied the heat transfer of viscoelastic hybrid nanofluids

(a mixture of MWCNTs and SWCNTs) flowing fractionally unsteadily through a Darcy porous medium across an inclined surface. Khan et al. [62] explained a utilization of fractional derivatives in an MHD nanofluid's Darcy medium natural convective flow.

Recent experimental investigations have demonstrated that combining multiple types of nanoparticles in a base fluid to form ternary nanofluids can significantly enhance their thermophysical properties compared to mono- or binary nanofluids. For instance, Ali et al. [63] and Nadooshan et al. [64] demonstrated that the synergistic interaction between dissimilar nanoparticles enhances energy transport mechanisms due to variations in particle size, shape, and thermal conductivities. In particular, ternary nanofluids such as $Cu - Al_2O_3 - TiO_2$/water and $Fe_3O_4 - CuO - MWCNTs$/ethylene glycol exhibited substantially higher effective thermal conductivities than their binary or single-component counterparts. This enhancement arises from improved phonon transport, reduced thermal boundary resistance, and increased Brownian motion contributions, which also induce favorable micro-convective effects. However, these benefits come with altered viscosity behavior: depending on nanoparticle concentration and temperature, viscosity may increase nonlinearly, which is particularly relevant for viscoelastic fluids, such as those modeled by the Maxwell and Williamson models. These rheological modifications affect flow resistance and momentum diffusivity, making it crucial to model such ternary systems using advanced constitutive frameworks.

The present study selects a ternary nanoparticle configuration due to its potential to simultaneously exploit high thermal conductivity ($e.g., Cu, Al_2O_3$), chemical stability ($e.g., TiO$), and magnetic field responsiveness ($e.g., Fe_3O_4$). Such combinations are especially beneficial in magneto-thermal environments, where field-controlled convection is desired, as in magnetic refrigeration or targeted heat delivery systems. Furthermore, the complex interplay between nanoparticle dispersion, thermophoresis, and Brownian motion—captured via fractional calculus—necessitates the integration of multiphase particle dynamics, which is effectively represented in the ternary formulation. While most theoretical studies focus on simplified nanofluid models, incorporating this ternary approach within a fractional viscoelastic micropolar framework provides a more realistic and predictive model, well aligned with experimental trends observed in nanofluid engineering. The suggested citations are included at the end of the references list.

This research examines the free convection Maxwell, Williamson, and micropolar nanofluid flow with the effect of magnetic field and radiation in porous media across an orthogonal plate while considering the influence of internal heating generation (IHG). Dimensionless equations were created using the system of partial differential equations. The symbolic software MAPLE 24 provided a numerical solution to the comparable equations using fractional numerical analysis. Graphical representations are used to display the distributions of velocity, rotational velocity, concentration profile, temperature profile, skin friction, Nusselt number, and Sherwood number. These results indicate that Williamson nanofluids outperform Maxwell micropolar fluids in terms of heat and mass transfer due to their shear-thinning properties, which enhance fluid flow and transfer efficiency.

Prior studies on fractional free convection in porous media have typically examined single rheological models or isolated transport effects, which prevents direct, like-for-like

comparisons of heat-transfer performance across Maxwell (elastic), Williamson (shear-thinning), and micropolar (micro-rotation) fluids under a common framework. Methodologically, existing works often lack rigorous stability or convergence analyses, grid independence checks, and broad benchmarking against established fractional solutions, which limits reproducibility and credibility. In addition, simplifying assumptions such as constant properties, uniform heat generation, or neglected induced magnetic fields are frequently adopted without justification, while derivations involving fractional operators and similarity transforms are presented in dense form, hindering transparency. Furthermore, rheology-specific physics—such as clear contrasts between elasticity and shear thinning, or the microstructural role of spin/vortex viscosity—has often been underexplored, leaving the mechanisms behind observed Nusselt number trends only partially resolved.

2. Novelty and Research Gap

The novelty of the present work lies in developing a unified time-fractional framework that simultaneously treats Maxwell, Williamson, and micropolar nanofluids within a porous medium under the combined effects of magnetic field, thermal radiation, and internal heat generation. This approach enables direct and consistent comparisons of heat-transfer behavior across different fluid models, which has not been systematically reported before. By incorporating Caputo fractional derivatives, the study captures memory effects in transient convection, while the numerical scheme ensures stability, convergence, and reproducibility. Physically, the analysis provides new insights into how elasticity, shear-thinning, and microrotation mechanisms interact with fractional-order dynamics to shape boundary-layer development and Nusselt number evolution in porous media systems, thereby offering guidance for the optimal selection of nanofluids in thermal management applications.

3. Assumptions

(i) The flow is assumed to satisfy the boundary layer approximation, meaning that velocity and temperature gradients normal to the plate dominate over those in the tangential direction.

(ii) The Boussinesq approximation is applied, where fluid density is treated as constant except in the buoyancy term of the momentum equation.

(iii) The porous medium is homogeneous, isotropic, and fully saturated, with resistance modeled using a Darcy-type drag force.

(iv) Thermophysical properties such as viscosity, thermal conductivity, and specific heat are assumed to remain constant throughout the flow domain.

(v) A uniform magnetic field is applied perpendicular to the flow, and any induced magnetic field is neglected due to the assumption of a low magnetic Reynolds number.

(vi) Thermal radiation is included using the Rosseland diffusion approximation, which is valid for optically thick media.

(vii) The fluid is treated as micropolar, allowing microrotation effects and couple stresses to be included in the model.

(viii) Internal heat generation is assumed to be uniform and constant throughout the fluid domain.

(ix) Fractional time derivatives in the Caputo sense incorporate memory and hereditary effects relevant to viscoelastic and non-Newtonian fluid behavior.

(x) Similarity transformations are employed to convert the governing partial differential equations into a set of ordinary differential equations, simplifying the numerical solution.

The assumptions of constant thermophysical properties, uniform heat generation, and negligible induced magnetic fields are reasonable for dilute nanofluids with small particle loading and moderate temperature differences, where property variations are minimal. Uniform volumetric heat generation effectively models distributed energy sources in porous structures, while the low magnetic Reynolds number ($Re_m \ll 1$). Typically, the nanofluids justify neglecting induced magnetic fields. These simplifications are standard in nanofluid convection studies, ensuring analytical tractability without compromising the essential physics.

4. Problem Formulation

The study of Maxwell, Williamson, and micropolar nanofluid magneto-natural convection flow via an orthogonal permeable plate in a saturated porous medium is considered. The impact of external heat radiation is also considered to enhance the thermal characteristics of the nanoliquid. A consistent magnetic field also takes the conducting material into account. To enhance the nanofluid's thermal properties, the effect of external thermal radiation is considered. Fig.1 illustrates the configuration of the flow and coordinate system. Let's assume that u, v are the components of the velocity along x- and y-axis, where x represents the plate's distance and y represents the plate's normal distance. The parameters are as follows: T and C are temperature and nanoparticle concentration, T_w and C_w are respectively the plate's temperature and concentration, T and C are respectively the ambient temperature and ambient concentration. With the boundary layer and Boussinesq approximations taken into account, the governing equations of this system are given by [**? ? ? ?**];

$$\frac{\partial u}{\partial x} + \frac{\partial v}{\partial y} = 0, \tag{1}$$

$$u\frac{\partial u}{\partial x} + v\frac{\partial u}{\partial y} = (\frac{\mu + k}{\rho})\frac{\partial^2 u}{\partial y^2} + \frac{k}{\rho}\frac{\partial N}{\partial y} - \frac{\sigma B_0^2}{\rho} - \frac{\mu u}{\rho K} + \sqrt{2}\Gamma v\frac{\partial u}{\partial y}\frac{\partial^2 u}{\partial y^2}$$

$$-\lambda_1[u^2\frac{\partial^2 u}{\partial x^2}+2uv\frac{\partial^2 u}{\partial x\partial y}+v^2\frac{\partial^2 u}{\partial y^2}]$$
$$+\frac{g^*}{\rho}[\rho\beta_T(1-C_\infty)(T-T_\infty)-(\rho-\rho_p)(C-C_\infty)], \tag{2}$$

$$u\frac{\partial N}{\partial x}+v\frac{\partial N}{\partial y}=\frac{\gamma}{jp}\frac{\partial^2 N}{\partial y^2}-\frac{k}{jp}(2N+\frac{\partial u}{\partial y}), \tag{3}$$

$$u\frac{\partial T}{\partial x}+v\frac{\partial T}{\partial y}=\alpha^*[\frac{\partial^2 T}{\partial y^2}]+\tau[D_B\frac{\partial C}{\partial y}\frac{\partial T}{\partial y}+\frac{D_T}{T_\infty}(\frac{\partial T}{\partial y})^2]+\frac{1}{\rho C_p}(q^m-\frac{\partial q_r}{\partial y}), \tag{4}$$

$$u\frac{\partial C}{\partial x}+v\frac{\partial C}{\partial y}=D_B[\frac{\partial^2 T}{\partial y^2}]+\frac{D_T}{T_\infty}(\frac{\partial T}{\partial y})^2, \tag{5}$$

As long as the following boundary requirements are true, see Mansour et al. [**?**];

$$u=0,v=0,T=T_w(x)=T_\infty+DT^\lambda,C=C_w,N=-n^*\frac{\partial u}{\partial y}\quad at\quad y=0, \tag{6}$$

$$u=0,T=T_\infty,C=C_\infty,N=0\quad as\quad y=\infty, \tag{7}$$

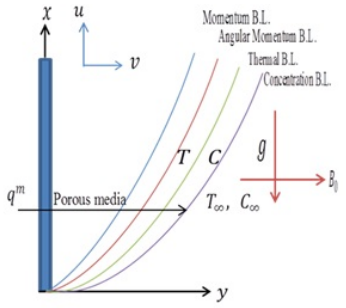

Figure 1: Configuration of the micropolar nanofluid.

Given that α^* represents the thermal diffusivity, C_p denotes the fluid's heat capacity, and β denotes the fluid's thermal expansion coefficient, $\beta_T,\mu,\rho,D_T,\rho_p,\tau$ and D_B are volumetric expansion, viscosity, density coefficients, thermophoresis parameter, nanoparticle mass density, the ratio of between heat capacity of nanofluid and nanoparticle, nanoparticle mass diffusivity, N is the angular velocity, k is the vortex viscosity, q^m is the fluid's internal heat generation (IHG), g^* is the gravity, B_0 is the strength of the magnetic field, K is the porous medium, γ is the spin gradient's viscosity, j is the density of microinertia, is a fractional parameter, Γ is a Williamson nanofluid parameter, λ_1 is a Maxwell nanofluid parameter (relaxation time of the fluid), σ is an electrical conductivity, and n^* is a constant. The radiative heat flux term $q_r=-\frac{4\sigma^*}{3k^*}\frac{\partial T^4}{\partial y}$, k^* is the coefficient of mean

absorption, σ^* is the Stefan-Boltzmann constant. By applying the Taylor expansion and increasing T^4 for the surrounding temperature T_∞, we arrive at $T^4 = -3T_0^4 + 4T_0^3T$.

Range of parameters and justification: Previous experimental and numerical studies of porous convection and nanofluid heat transfer guide the chosen ranges for the dimensionless parameters. The magnetic parameter ($M = 02$) reflects low-to-moderate magnetic Reynolds number regimes typical of electrically conducting nanofluids. The Darcy number ($Da = 110$) represents porous media from moderately resistive to highly permeable structures. Grashof numbers ($Gr = 0.2-1.0$) are selected to capture laminar natural convection regimes before transition to turbulence. The buoyancy ratio ($Nr = 02$) encompasses both stabilizing and destabilizing solutal buoyancy conditions. Micropolar vortex viscosity (R) and spin viscosity (B) are taken in the range 02 to illustrate weak-to-strong microrotation coupling, consistent with micropolar theory. The Prandtl number ($Pr = 0.77$) corresponds to working fluids such as air, water, and light oils, while the Schmidt number ($Sc = 110$) reflects typical nanoparticle diffusivities. Brownian ($Nb = 0.10.5$) and thermophoresis ($Nt = 0.10.5$) parameters are chosen within the range reported in nanofluid literature to represent moderate nanoparticle transport effects. These ranges ensure that the simulations remain physically realistic and comparable to existing fractional and non-fractional convection studies.

5. Some important concepts of fractional calculus

Definition 1. *The gamma function* $\Gamma(x)$ *is defined by the integral* $\Gamma(x) = \int_0^\infty t^{x-1}e^{-t}dt$. *And it satisfies the following functional equation* $\Gamma(n+1) = n\Gamma(n) = n!$, $\Gamma(\frac{1}{2}) = \pi$.
The gamma function is given by the limit $\lim_{n\to\infty} \frac{n!n^x}{x(x+1)(x+2)...(x+n)}$.

Definition 2. *Caputo's fractional derivative is defined as:*

$$ {}_a^C D_\tau^\alpha f(\tau) = \begin{cases} \frac{1}{\Gamma(\alpha-n)}\int_a^\tau (\tau-t)^{n-\alpha-1} f^{(n)}(t)dt, & n-1 < \alpha < n, n \in \mathbb{N}, \\ \frac{d^n f(\tau)}{dt^n}, & \alpha = n \in \mathbb{N}. \end{cases} $$

For $n = 1$ *and lower terminal* $a = 0$, *the fractional derivative is* ${}_0^C D_\tau^\alpha f(\tau) = \frac{1}{\Gamma(\alpha-1)}\int_0^\tau \frac{f'(t)dt}{(\tau-t)^\alpha}, 0 < \alpha < n$.

Definition 3. *Riemann-Liouville fractional derivative is given by:*

$$ {}_aD_t^\alpha f(\tau) = \begin{cases} \frac{1}{\Gamma(\alpha-n)}\frac{d^n}{dt^n}\int_a^t \frac{f(t)}{(\tau-t)^{\alpha-n+1}}dt, & n-1 < \alpha < n, n \in \mathbb{N}, \\ \frac{d^n f(\tau)}{t^n}, & \alpha = n \in \mathbb{N} \end{cases} $$

6. Non-Dimensionalization in an environment with fractions

6.1. Similarity transformations

For the investigation of a steady magneto-natural convection flow of fractional Maxwell, Williamson, and micropolar nanofluid across an orthogonal permeable plate in a saturated porous medium, the similarity transformations are;

$$\begin{aligned}\eta^{\alpha} &= \frac{y^{\alpha}}{x\Gamma(\alpha+1)}(\frac{Gr}{4})^{\frac{1}{4}}, \Psi = \Psi(x,y) = 4(\frac{Gr}{4})^{\frac{1}{4}} f(\eta^{\alpha}), N = \frac{4\nu}{x^2}(\frac{Gr}{4})^{\frac{3}{4}} g(\eta^{\alpha}), \theta(\eta) = \frac{T-T_{\infty}}{T_w - T_{\infty}},\\ &\Phi(\eta)\frac{(C-C_{\infty}}{C_w - c_{\infty}}, q^m = \frac{k(T_w - T_{\infty})}{x^2}(\frac{Gr}{4})^{\frac{1}{2}} e^{-\eta}, Gr = \frac{(g^{*}\beta_T(1-C_{\infty})(T_w - T_{\infty})x^3}{\nu^2},\\ &u = \frac{4\nu}{x}(\frac{Gr}{4})^{\frac{1}{2}}\frac{y^{\alpha-1}}{\Gamma(\alpha)} f^{\alpha}(\eta^{\alpha}), v = -\frac{(\lambda+3)\nu}{x}(\frac{Gr}{4})^{\frac{1}{4}} f - (\lambda-1)\nu\frac{1}{x^2}(\frac{Gr}{4})^{\frac{1}{4}}\frac{y^{\alpha}}{\alpha\Gamma(\alpha)} f^{\alpha}(\eta^{\alpha}) \quad (8)\end{aligned}$$

It is noted that the choice of $\lambda = 1$ is not arbitrary but essential to maintain self-similarity in the fractional framework. In general, the imposed wall heat flux scales as $q_w(x) \propto x^{\lambda-1}$, which, under similarity transformation, introduces streamwise dependence unless $\lambda = 1$. By enforcing this condition, the boundary condition simplifies to a constant heat flux, thereby eliminating residual $x-$ terms and allowing the governing PDEs with Caputo derivatives to reduce to a closed system of ODEs in . Physically, the case $\lambda = 1$ represents a uniformly heated plate—a widely accepted model in porous media and boundary-layer studies, where heaters or embedded heat sources provide a near-uniform surface flux. This idealization not only preserves mathematical tractability but also facilitates direct comparisons between Maxwell, Williamson, and micropolar nanofluids under identical heating conditions.

An imposed magnetic field, vortex viscosity parameters, and Darcy number should not depend on x to obtain similarity solutions. So, taking $Gr_x \sim x^{\lambda+3}$, then $\lambda = 1.0$, and we deduce that the heat flow to the wall is uniform at $\lambda = 1.0$. By substituting Equation (8) into Equations (1)-(4) and with boundary conditions (5), we get: obtaining the similarity solutions, $\lambda = 1.0$ implies that a uniform heat flux is applied to the wall and that the flow of heat is applied uniformly to the wall. Where α is a fractional parameter since $0 < \alpha \leq 1$

We verify that the fractional transform satisfies the continuity equation by adding Eqns. (8) in Eq. (1). After utilizing some computation and substituting Eq. (8) into Eqns. (1-5), the following fractional differential equations are produced:

$$\begin{aligned}&(1+R)[\alpha\eta^{\alpha-1} f^3\alpha] + (\lambda+3)ff^2\alpha - [2(\lambda+1) + 2\sqrt{2}\frac{(\lambda+3)(\alpha-1)}{/\alpha}\eta^{-\alpha} ff^{\alpha} - \frac{2}{Da}\frac{\eta^{-\alpha+1}}{\alpha} f^{\alpha}\\ &-M\frac{\eta^{-\alpha+1}}{\alpha} f^{\alpha} + R\frac{\eta^{-\alpha+1}}{\alpha} g^{\alpha} + \frac{\eta^{-2\alpha+2}}{\alpha^2}(\theta - Nr) + We\alpha^3\eta^{3\alpha-3}[f^2\alpha f^3\alpha]\\ &-\beta\alpha\eta^{\alpha-1}[4(\lambda+1)(\lambda-1) - 4\frac{(\alpha-1)(\lambda+1)(\lambda-1)}{\alpha}(f^{\alpha})^3\\ &3(\lambda-1)^2 + 2(\lambda+1)(\lambda-1) - 2(\lambda-1)(3\lambda+1)\eta^{\alpha}(f^{\alpha})^2 f^{2\alpha}\\ &-2(\lambda+3)(3\lambda+1)ff^{\alpha} f^{2\alpha} + (\lambda+3)^2 f^2 f^{3\alpha}] = 0, \quad (9)\end{aligned}$$

$$(1-\frac{R}{2}\alpha\eta^{\alpha-1})g^{2\alpha}+\frac{R}{2\eta}(\alpha-1)g^{\alpha}(\lambda+3)fg^{\alpha}-(3\lambda+1)f^{\alpha}g$$
$$-RB(2g+(\alpha-1)\eta^{-1}f^{\alpha}+\alpha\eta^{\alpha-1}f^{2\alpha})=0, \tag{10}$$

$$(1+\frac{4}{3}Rd)[4(\alpha-1)\eta^{-1}\theta^{\alpha}+\alpha\eta^{\alpha-1}\theta^{2}\alpha]+\frac{1}{\alpha\eta^{\alpha-1}}de^{-\eta}-4\lambda Prf^{\alpha}\theta+(\lambda+3)Prf\theta^{\alpha}$$
$$+Pr[\alpha\eta^{\alpha-1}Nb\phi^{\alpha}\theta^{\alpha}+\alpha\eta^{\alpha-1}Nr(\theta^{\alpha})^{2}]=0, \tag{11}$$

$$\alpha\eta^{\alpha-1}\phi^{2\alpha}+(\lambda+3)Scf\phi^{\alpha}+2(\alpha-1)\eta^{-1}\phi^{\alpha}+\frac{Nt}{Nb}[\alpha\eta^{\alpha-1}\theta^{2\alpha}+2(\alpha-1)\eta^{-1}\theta^{\alpha}]=0. \tag{12}$$

Under the following conditions;

$$f(0)=f'(0)=0,\theta(0)=1,\phi(0)=1,g(\eta)\to -n^{*}f'',\quad at\quad \eta=0, \tag{13}$$

$$f'(\eta)\to 0,\theta(\eta)\to 0,\phi(\eta)\to 0,g(\eta)=0,\quad as\quad \eta\to\infty. \tag{14}$$

Given that Q^{*} is constant ($Q^{*}=0$ denotes the absence of internal heating generation (WIHG),and $Q^{*}=1$ the presence of internal heating generation (IHG)), $\beta=\frac{\nu}{x^{2}}(\frac{Gr}{4})^{\frac{1}{2}}\lambda_{1}, M=\frac{(\sigma B_{0}^{2})}{\mu x^{2}}(\frac{Gr}{4})^{\frac{-1}{2}}, Da=\frac{2K}{x^{2}}(\frac{Gr}{4})^{\frac{1}{2}}, We=\frac{(4\sqrt{2}\Gamma\nu)}{x^{2}}(\frac{Gr}{4})^{\frac{3}{4}}, Sc=\frac{\nu}{D_{B}}, Pr=\frac{\nu}{\alpha^{*}}, Nb=\frac{\tau D_{B}(C_{w}-C_{\infty})}{\nu}, Nt=\frac{\tau D_{T}(T_{w}-T_{\infty})}{T_{\infty}\nu}, Nr=\frac{(\rho_{p}-\rho)(C_{w}-C)}{\rho\beta_{T}(T_{w}-T_{\infty})(1-C_{\infty})}, Rd=\frac{4\sigma^{*}T^{3}{}_{\infty}}{kk^{*}}, R=\frac{k}{\mu}$, and $B=\frac{x^{2}}{j}(\frac{Gr}{4})^{\frac{1}{2}}$ These are respectively the Maxwell parameter, magnetic field, Darcy number, Williamson parameter, Schmidt number, Brownian number, thermophoresis number, buoyancy ratio, radiation parameter, and material coefficients. Additionally significant and necessary to consider are the C_{f} skin friction coefficient, the Nusselt number Nu, and the Sherwood number Sh, which

$$\tau_{w}=-\mu(1+\frac{R}{2}+\beta)(1+\frac{\Gamma}{2}\frac{\partial u}{\partial y})\frac{\partial u}{\partial y}|_{y=0}, q_{w}=-(k\frac{\partial T}{\partial y}-q_{r})|_{y}=0, q_{m}=-D_{B}\frac{\partial C}{\partial y}|_{y}=0. \tag{15}$$

Equation (8)'s dimensionless transformation gives us the following;

$$4(\frac{Gr}{4})^{\frac{1}{4}}C_{f}=(1+\frac{R}{2}+\beta)(f''(\theta)+\frac{We}{2}f''(\theta)), (\frac{Gr}{4})^{\frac{-1}{4}}Nu=-(1+\frac{4}{3}Rd)\theta'(0), (\frac{Gr}{4})^{\frac{-1}{4}}, Sh=-\phi'(0). \tag{16}$$

7. Numerical method

The governing nonlinear differential equations are converted into ordinary differential equations, which are then numerically solved using the symbolic software Maple 24. The domain is truncated at a sufficiently large value of the similarity variable $\eta = \eta^{\infty}$ (typically $\eta^{\infty} = 810$), ensuring negligible residual gradients beyond this point. The governing equations are discretized using a uniform step size of $\Delta\eta = 0.01$, which was determined based on mesh refinement studies to strike a balance between computational cost and solution accuracy. Convergence is achieved when successive iterations differ by less than 10^{-5} in all primary variables (dimensionless velocity, angular velocity, temperature, and concentration profiles). The authors employ a fully implicit finite difference method (FDM) combined with the Caputo fractional time derivative to solve the governing fractional-order partial differential equations. The key motivation for this choice is to ensure numerical stability, robustness in stiff regimes, and compatibility with physically meaningful initial conditions.

(i) Caputo Fractional Derivative Discretization; The Caputo derivative of order $0 < \alpha < 1$ for a function $f(t)$ is defined as: ${}^{C}D_t^{\alpha} f(t) = \frac{1}{\Gamma(\alpha-1)} \int_0^t \frac{f'(\xi)d\xi}{(t-\xi)^{\alpha}}$. In discrete form, using the $L1$ approximation on a uniform temporal grid with time step Δt, the Caputo derivative at time level n is approximated by:
${}^{C}D_t^{\alpha} f(t) = \frac{1}{\Gamma(2-\alpha)} \frac{1}{\Delta t^{\alpha}} \sum_{k=0}^{n-1} a_k^n (f^{k+1} - f^k)$,
$a_k^n = (n-k)^{1-\alpha} - (n-k-1)^{1-\alpha}$. This scheme preserves accuracy while capturing non local temporal effects.

(ii) Spatial Discretization and System Assembly; For the spatial discretization, the authors use second-order central differences: For a function f, the second derivative at node i is approximated as: $\frac{\partial f^2}{\partial r}|_i \approx \frac{(f_(i+1)-2f_i+f_(i-1))}{\Delta r^2}$.
First-order derivatives are approximated by centered or one-sided differences depending on boundary proximity. The resulting discrete equations form a tridiagonal system at each time step, which is solved using the Thomas algorithm, an efficient direct solver for tridiagonal matrices. The stability of the finite difference scheme with Caputo fractional derivative was verified using a von Neumann analysis, which confirmed that the amplification factor remains bounded ($G1$) for $0 < \alpha \leq 1$, indicating unconditional stability. Convergence was tested through mesh refinement in both spatial and temporal directions, with successive reductions in $\Delta\eta$ and Δt producing changes of less than 12% in the wall gradients $-f''(0,t)$ and $-\theta'(0,t)$, demonstrating grid independence. The scheme exhibits first-order accuracy in time and second-order accuracy in space, consistent with fractional finite difference formulations. For validation, the computational domain was extended from $\eta_{\infty} = 6$ to $\eta_{\infty} = 10$, and results remained unchanged within 1%, confirming the adequacy of the truncation boundary. Furthermore, in the limiting case of $\alpha = 1$,the present results show excellent agreement with established integer-order convection studies,while comparisons with analytical solutions of the fractional diffusion equation yield errors below 2%. The fully implicit finite difference scheme combined with the Caputo fractional

derivative offers several advantages for modeling time-fractional porous media flows. First, it is unconditionally stable under von Neumann analysis, which ensures reliability even in stiff parameter regimes. Second, the method achieves first-order accuracy in time and second-order accuracy in space, striking a balance between efficiency and precision. Third, the $L1$ discretization effectively captures memory and hereditary effects inherent in fractional-order models, which classical schemes cannot represent. Moreover, the tridiagonal system solved by the Thomas algorithm makes the approach computationally efficient for large-scale simulations. Finally, the method is easily extendable to more complex boundary conditions, variable properties, and other fractional constitutive laws, giving it flexibility for future research.

8. Results and Discussion

This work presents a similarity solution for the free convection of Maxwell and Williamson micropolar nanofluid flow along a vertical plate within a porous medium. The analysis includes cases with and without internal heat generation. $Q^* = 1.0$ (IHG) and $Q^* = 0.0$ (WIHG). The skin friction and Nusselt number are compared to the published results of Mansour et al. [**?**] in Table 1, to confirm the accuracy of our current numerical results for various values. The comparison of these results shows that they are excellent and nearly perfect. In the current work, we choose the case of n=0, which refers to concentrated flows of particles in which the microelements near the wall cannot rotate. Furthermore, the effects of the governing parameters on the heat and mass transfer characteristics of Williamson and Maxwell micropolar nanofluids are analyzed for both cases. All simulations assume that a uniform heat flow is applied to the wall, and the wall receives heat uniformly. Williamson micropolar nanofluids exhibit shear-thinning properties, whereas Maxwell Micropolar nanofluids demonstrate viscoelastic behavior. The numerical results are analyzed graphically. Figures 2 (a) and (b) reveal the impact of Darcy number and

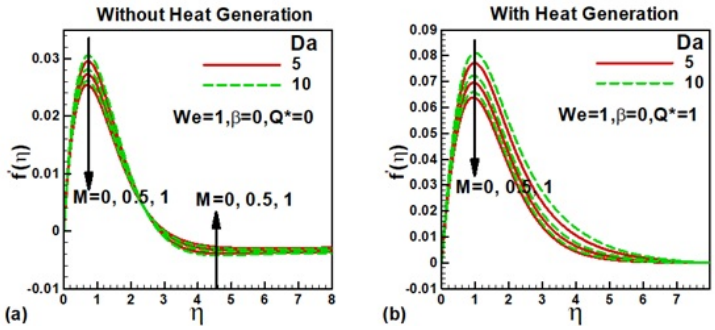

Figure 2: Effects of Darcy number and magnetic field on dimensionless velocity of Williamson micropolar nanofluid.

magnetic field on dimensionless velocity in the free convection of Williamson-micropolar nanofluids across a vertical plate within porous media. At $We = 1$, the Williamson–micropolar nanofluid exhibits moderate non-Newtonian behavior, which reduces viscosity

and enhances velocity under shear, as shown in Fig. 2 (a). Increasing magnetic field strength Mgenerates a Lorentz force opposing the flow, decreasing the peak velocity and thickening the boundary layer. This damping is stronger at lower Darcy numbers, where reduced permeability limits fluid motion. In the absence of a magnetic field, the velocity reaches its maximum, reflecting buoyancy-driven convection without electromagnetic resistance. When heat generation is included, as shown in Fig. 2(b), additional thermal energy decreases viscosity and enhances buoyancy, which increases velocity and produces a thinner boundary layer compared to the non-heating case. The magnetic field still suppresses velocity, and its damping effect outweighs the acceleration from heat generation. Although velocities are overall higher than in Fig. 2(a), the Lorentz force remains the dominant controlling factor.

These results highlight the competing effects of permeability, magnetic damping, and internal heating in porous media. High Darcy numbers and heat generation promote stronger convection, which is desirable for applications such as geothermal systems, catalytic reactors, and porous heat exchangers. Conversely, magnetic fields, while useful for flow control and stability, can substantially suppress velocity and limit heat transfer. This interplay suggests that optimizing porous media systems requires balancing permeability and internal heating with magnetic control, depending on whether the goal is enhanced cooling or regulated transport. The impacts of the Grashof number (Gr) and buoy-

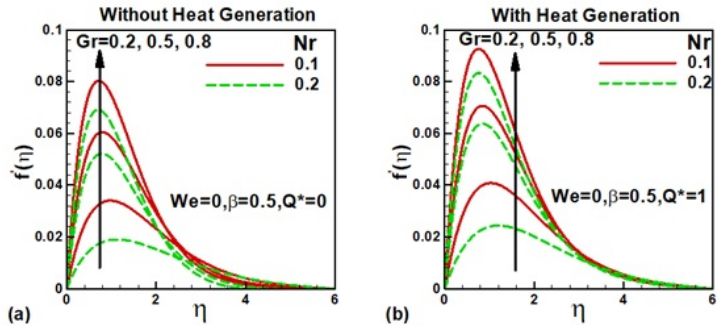

Figure 3: Effects of Grashof number and buoyancy on dimensionless velocity of Maxwell micropolar nanofluid.

ancy (Nr) are explained in Figs. 3 (a) and (b) in the absence and presence of internal heat generation for Maxwell micropolar nanofluid. In Fig. 3(a), for Maxwell–micropolar nanofluid, increasing the Grashof number (Gr) strengthens buoyant forces, which enhance velocity near the surface and intensify convection. In contrast, the buoyancy ratio parameter (Nr) exerts a stabilizing effect by counteracting the upward thermal buoyancy, thereby reducing velocity close to the wall. The velocity profile peaks near the plate and decreases toward the boundary layer edge, reflecting the competition between buoyant acceleration and viscous resistance. With internal heat generation, as shown in Fig. 3(b), the overall velocity increases, and the boundary layer becomes thinner because the added thermal energy reduces viscosity and enhances buoyancy. The effects of Grand Nrremain consistent: Grpromotes stronger near-wall acceleration, while Nrmoderates this growth by resisting excessive upward motion. The combined influence of buoyancy and

internal heating intensifies convection but remains regulated by the stabilizing role of Nr. These results emphasize the importance of buoyancy control in porous media flows. A higher Grashof number can enhance natural convection, which is beneficial in applications such as solar collectors, geothermal reservoirs, and porous heat exchangers. However, the buoyancy ratio parameter helps prevent unstable or excessive acceleration, contributing to flow stability. Internal heat generation further enhances convection efficiency, but it requires a careful balance to avoid thermal runaway in systems such as catalytic reactors or nuclear waste storage. Figures 4 (a) and (b) illustrate the distribution of microrotation

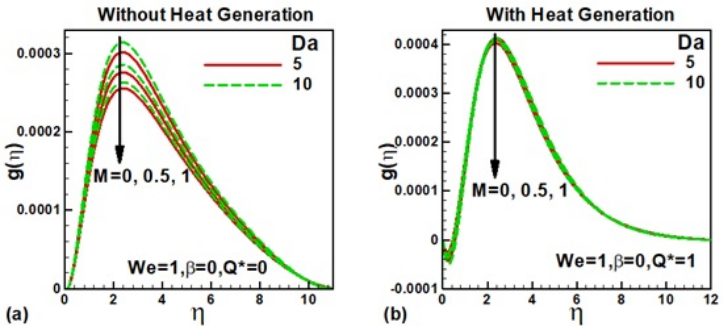

Figure 4: Effects of Darcy number and magnetic field on dimensionless angular velocity of Williamson micropolar nanofluid.

for Williamson micropolar nanofluid in a vertical porous channel under varying magnetic field strength $M = 0, 0.5, 1$ and Darcy number $Da = 5, 10$, with and without internal heat generation. In the absence of internal heat generation, for Williamson–micropolar nanofluid, the microrotation profile g( )rises sharply near the plate, reaches a peak, and gradually decays toward the boundary layer edge as microrotation weakens. Increasing magnetic field strength ($M = 01$) lowers the peak angular velocity, highlighting the suppressive effect of the Lorentz force on spin motion. A higher Darcy number ($Da = 10$) slightly enhances angular velocity compared to Da=5, but this influence is much weaker than that of the magnetic field. With internal heat generation ($Q^* = 1$), microrotation peaks increase relative to the non-heating case because thermal energy reduces resistance and promotes rotational motion of microelements. The Darcy number shows negligible influence, as curves for Da=5and Da=10 almost overlap, demonstrating that thermal effects dominate over permeability. Although increasing Mstill damps rotation, angular velocity remains higher than in Fig. 4(a), confirming that heat generation offsets part of the magnetic suppression. Microrotation reflects the spin of suspended particles and fluid microstructures, which influences effective viscosity and momentum transfer in micropolar fluids. Suppression by magnetic fields suggests that MHD control can regulate microstructural dynamics, stabilizing flow when needed. Conversely, internal heat generation enhances microrotation, improving rotational energy exchange, which may contribute to higher effective thermal transport. These results are relevant for magnetized porous heat exchangers, electro-conductive nanofluid systems, and micro-scale energy devices, where balancing spin effects can optimize both stability and heat transfer performance. Figures

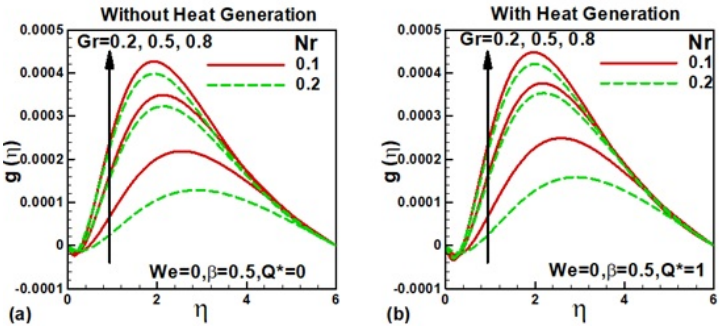

Figure 5: Effects of Grashof number and buoyancy on dimensionless angular velocity of Maxwell micropolar nanofluid.

5 (a) and (b) illustrate the impact of the Grashof number (Gr) and buoyancy (Nr) on the dimensionless angular velocity $g()$ of Maxwell micropolar nanofluids without and with heat generation. For Maxwell–micropolar nanofluid, the angular velocity $g()$ increases near the plate due to thermal and concentration gradients, reaches a maximum at an intermediate distance, and then declines as viscous forces dominate toward the boundary layer edge. A higher Grashof number (Gr) strengthens buoyancy-driven convection, producing greater angular velocity peaks, while the buoyancy ratio parameter (Nr) counteracts this effect by stabilizing the flow and reducing maximum values. In the presence of heat generation, the angular velocity peaks are noticeably higher than in the non-heating case, as shown in Fig. 5(b). Added thermal energy reduces resistance and intensifies buoyancy forces, leading to stronger microrotation and enhanced convective activity. As before, Grpromotes higher angular velocity, while Nrmoderates it, but the overall profiles remain elevated because of the internal energy source. Microrotation reflects the rotational behavior of suspended particles and fluid microstructures, which influences effective viscosity and momentum transport in porous media flows. Enhancements from Gr and internal heating suggest that convection can be boosted in applications such as geothermal reservoirs, porous heat exchangers, and catalytic reactors, where more vigorous microstructural activity improves heat and mass transfer. Conversely, the moderating effect of Nrhighlights its role in maintaining flow stability, a critical factor in designing thermally loaded porous systems. The

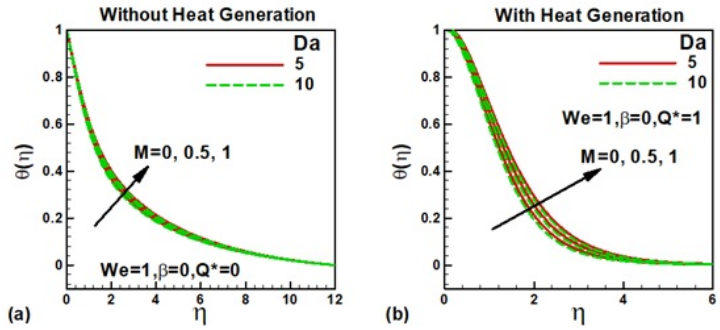

Figure 6: Effects of Darcy number and magnetic field on dimensionless temperature of Williamson micropolar nanofluid.

influence of different governing parameters on the dimensionless temperature of Williamson and Maxwell micropolar nanofluids is illustrated in Figs. 6-8 without and with heat generation in a porous medium. Figures 6 (a) and (b) show the effects of Darcy number and magnetic field on the dimensionless temperature of Williamson micropolar nanofluid. For Williamson–micropolar nanofluid, the Darcy number (Da) has minimal effect on the temperature field since porous resistance plays only a minor role in the absence of internal heating. The magnetic field, however, raises the dimensionless temperature inside the boundary layer. The Lorentz force suppresses fluid motion, reducing convective heat transport and causing heat to accumulate, which thickens and intensifies the thermal boundary layer. When heat generation is present, the thermal boundary layer becomes thinner due to the rapid temperature rise near the wall, as shown in Fig. 6(b). The additional thermal energy reduces fluid resistance and produces steeper gradients near the surface, thereby confining the heat distribution. Although the magnetic field continues to suppress motion and retain heat, the dominant effect of heat generation is enhanced near-wall heating, characterized by sharper temperature gradients.These results show that magnetic fields can trap heat and thicken thermal layers, which is useful for thermal insulation and controlled heating applications, while internal heat generation intensifies near-wall gradients that may enhance heat exchanger efficiency or catalytic processes. Balancing magnetic suppression and heat generation is therefore critical for designing porous media systems where both heat retention and transfer efficiency must be optimized. The effects of the

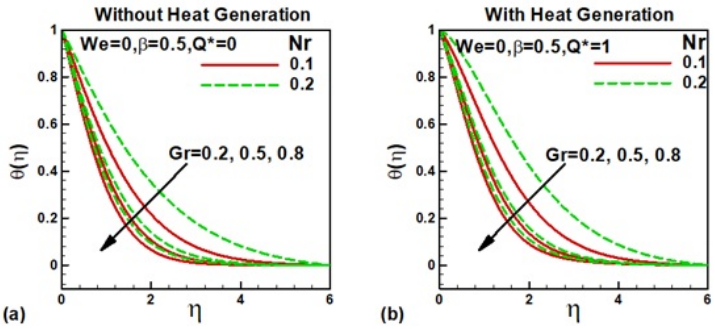

Figure 7: Effects of Grashof number and buoyancy on dimensionless temperature of Maxwell micropolar nanofluid.

Grashof Number and buoyancy on the dimensionless temperature of Maxwell micropolar nanofluid are demonstrated in Figs. 7 (a) and (b) in the absence and presence of heat generation, respectively. For Maxwell–micropolar nanofluid, increasing the Grashof number (Gr) enhances buoyancy-driven convection, which promotes stronger upward motion of the fluid. This results in lower temperatures near the wall, as hotter fluid is displaced and replaced by cooler fluid from the surroundings, thinning the thermal boundary layer. In contrast, a higher buoyancy ratio parameter (Nr) stabilizes the flow and traps heat inside the boundary layer, leading to higher temperature values and thicker profiles.When heat generation is included, the same trends of Gran and are observed: decreases the thermal profile by enhancing convective cooling, while increases it by resisting thermal

transport, as shown in Fig. 7(b). However, the overall change in thermal boundary layer thickness remains modest, indicating that heat generation primarily amplifies near-wall heating but does not significantly alter the balance between buoyancy-induced convection and stabilization by Nr.

These findings highlight the competing effects of buoyancy and stabilizing forces on thermal behavior in porous media. Larger Grva values promote cooling efficiency, which is advantageous in applications such as geothermal reservoirs and porous heat exchangers, while higher values enhance heat retention, beneficial for thermal insulation and controlled heating systems. The modest influence of heat generation suggests that external buoyancy control may be more effective than internal heating for regulating thermal performance in such systems. The effects of Brownian Motion and Thermophoresis param-

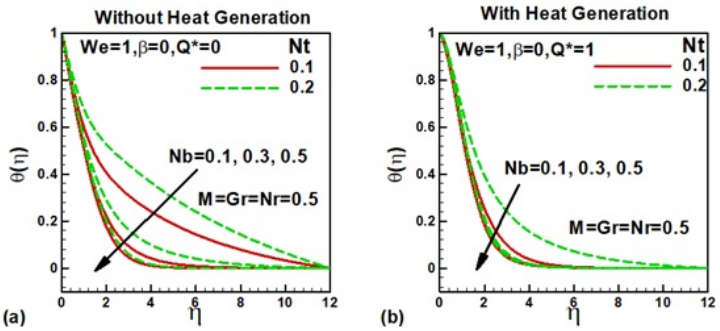

Figure 8: Effects of nanofluid parameters on dimensionless velocity of Williamson micropolar nanofluid.

eters on the dimensionless temperature of Williamson micropolar nanofluid are depicted in Figs. 8 (a) and (b). For Williamson–micropolar nanofluid, increasing the Brownian motion parameter (Nb) reduces the dimensionless temperature inside the thermal boundary layer, Fig. 8 (a). Enhanced nanoparticle diffusion transfers heat more efficiently to the base fluid, lowering temperature near the surface and accelerating thermal decay. In contrast, a higher thermophoresis parameter (Nt) raises the temperature profile, sicausing nanoparticles to migrate from hot regions to cooler zones, which in turn causes heat to accumulate near the wall and thicken the boundary layer. When internal heat generation is present, the influence of Nb and Nt remains similar, but the thermal boundary layer becomes thinner for larger Nb,as shown in Fig. 8 (b). Stronger Brownian motion leads to faster heat dissipation, resulting in sharper temperature gradients near the surface. Although Nt still increases the temperature by promoting heat accumulation near the wall, its effect is moderated by the enhanced near-wall gradients induced by both Brownian motion and internal heating. The interplay between Brownian motion and thermophoresis highlights the dual role of nanoparticles in heat transport. Stronger Brownian motion enhances cooling efficiency, which is advantageous for nanofluid-based heat exchangers and cooling devices, while thermophoresis contributes to localized heat buildup, useful for thermal storage and surface heating applications. The presence of internal heat generation further emphasizes how micro-scale particle dynamics can be tuned to optimize heat transfer in porous nanofluid systems. Figures 9-11 analyze the effects of governing parame-

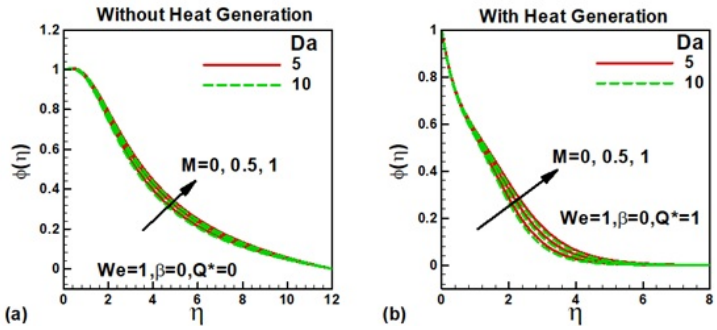

Figure 9: Effects of Darcy number and magnetic field on dimensionless concentration of Williamson micropolar nanofluid.

ters on the dimensionless concentration of Williamson micropolar nanofluid in the absence and presence of internal heat generation in a porous medium. The impact of the Darcy number and magnetic field on the dimensionless concentration of Williamson micropolar nanofluid is examined in Figs. 9 (a) and (b). For Williamson–micropolar nanofluid, the Darcy number (Da) shows little effect on the concentration distribution in the absence of internal heating, as permeability does not strongly influence convective mass transfer under these conditions. By contrast, applying a magnetic field increases nanoparticle concentration within the boundary layer. The Lorentz force opposes fluid motion, slowing down transport and causing nanoparticles to accumulate, which thickens the concentration boundary layer. When heat generation is included, both permeability and the magnetic field influence concentration profiles, as shown in Fig. 9(b). The Darcy number slightly alters concentration because porous resistance interacts with thermally induced gradients. Additional thermal energy steepens temperature and concentration gradients, which accelerates diffusion and leads to a thinner, more confined concentration boundary layer. Despite this thinning, the magnetic field continues to promote nanoparticle accumulation by damping the fluid motion.

These results demonstrate how magnetic fields and internal heating can be utilized to regulate the distribution of nanoparticles in porous nanofluids. Magnetic control favors nanoparticle trapping and stabilization, which may be advantageous in drug delivery, catalytic reactors, or controlled mixing systems. Conversely, heat generation enhances diffusion and accelerates mass transfer, which is helpful for porous heat exchangers and thermal energy storage devices where rapid transport is required. The effects of Grashof number and buoyancy on the dimensionless concentration of Maxwell micropolar nanofluid are examined in Figs. 10 (a) and (b) without and with internal heat generation. For Maxwell–micropolar nanofluid, increasing the Grashof number (Gr) lowers the concentration profile because stronger buoyancy enhances convection, which sweeps nanoparticles away from the wall. In contrast, a higher buoyancy ratio parameter (Nr) raises the concentration inside the boundary layer, as its stabilizing effect retains nanoparticles near the surface and slows their outward transport. With internal heat generation, the same opposing roles of Grand Nrare observed. However, the additional thermal energy increases gradients within the boundary layer, causing faster diffusion and sharper decay of concen-

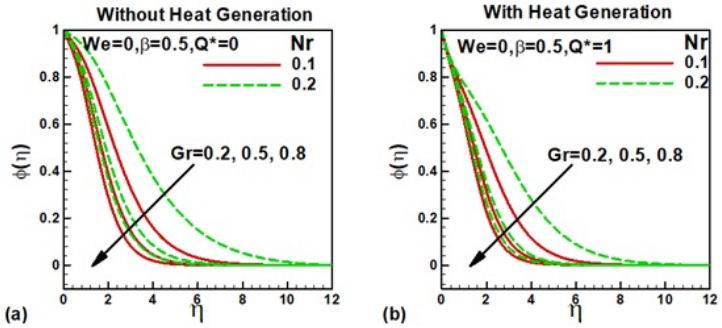

Figure 10: Effects of Grashof number and buoyancy on dimensionless concentration of Maxwell micropolar nanofluid.

tration near the wall. This results in a thinner concentration boundary layer compared to the non-heating case, even when buoyancy forces are present.

These trends reveal the balance between buoyancy-driven convection, which promotes nanoparticle transport away from surfaces, and stabilizing effects that enhance retention. In porous nanofluid systems, higher Grvalues improve mixing and mass transfer efficiency, while larger Nrfavors nanoparticle stability and controlled deposition. The influence of internal heat generation highlights its potential role in accelerating nanoparticle dispersion for thermal energy storage, porous catalytic reactors, and nanofluid-based cooling systems. Figures 11 display the effects of Brownian motion and thermophoresis on di-

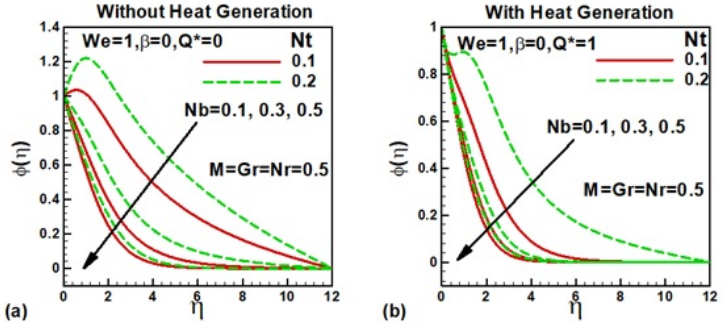

Figure 11: Effects of nanofluid parameters on dimensionless concentration of Williamson micropolar nanofluid.

mensionless concentration of Williamson micropolar nanofluid. For Williamson–micropolar nanofluid, increasing the Brownian motion parameter (Nb) lowers the nanoparticle concentration near the wall, Fig. 11 (a). Enhanced random motion promotes uniform dispersion throughout the fluid, reducing localized accumulation within the boundary layer. Conversely, a higher thermophoresis parameter (Nt) raises the concentration by driving nanoparticles from hotter zones toward cooler regions, leading to greater accumulation near the surface. When heat generation is present, thermal gradients within the boundary layer intensify, thereby amplifying thermophoretic migration, as shown in Fig. 11(b). This results in more substantial nanoparticle accumulation near the wall, thereby enhancing concentration profiles. For small Nb, the influence of Brownian dispersion is weaker,

allowing thermophoresis to dominate, which results in a thinner concentration boundary layer. At higher Nb, dispersion offsets this effect, maintaining a broader profile with more uniform particle distribution.

These results highlight the delicate balance between nanoparticle diffusion (Brownian motion) and directed migration (thermophoresis) in thermal porous systems. Brownian motion favors uniform mixing, which is beneficial for nanofluid cooling and mixing applications. In contrast, thermophoresis promotes surface accumulation, making it useful in targeted deposition, coating, and thermal storage systems. The influence of heat generation shows how thermal control can shift this balance, enabling system-specific optimization of nanoparticle behavior. Figures 12 and 13 investigate the behavior of skin friction for

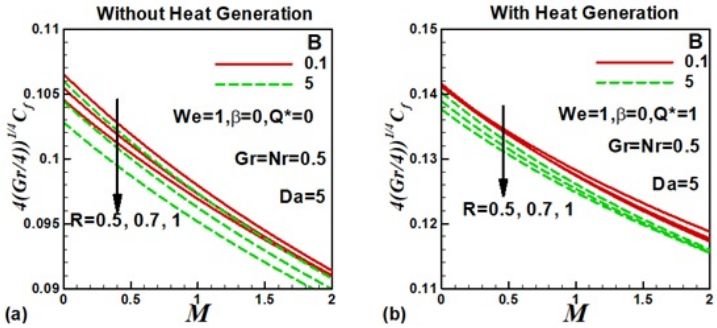

Figure 12: Variation of skin friction with magnetic field for several values of Vortex viscosity (R) and spin viscosity (B) parameters for Williamson micropolar nanofluid.

Williamson and Maxwell micropolar nanofluids along a vertical plate in a porous medium. The effects of magnetic field (M), Vortex Viscosity (R), and Spin Viscosity (B) parameters on skin friction are displayed in Figs. 12 (a) and (b) for Williamson micropolar nanofluid and in Figs. 13 (a) and (b) for Maxwell micropolar nanofluid. In Fig. 12(a), for the Williamson–micropolar nanofluid, the skin friction decreases with increasing magnetic field strength ( ) due to the Lorentz force opposing fluid motion and reducing the near-wall momentum. Higher vortex viscosity (R) also lowers skin friction by amplifying rotational resistance, which stabilizes the flow and weakens momentum transfer at the boundary. Similarly, increasing spin viscosity (B) resists microrotation of fluid microstructures, further restricting motion and contributing to reduced skin friction. In the presence of internal heat generation, the overall skin friction is higher compared to the non-heating case. Thermal energy raises fluid temperature and enhances buoyancy-driven acceleration, which increases near-wall velocity gradients and elevates surface friction. While magnetic field, vortex viscosity, and spin viscosity continue to act as suppressing factors, the effect of heat generation dominates, leading to stronger momentum near the wall and higher skin friction values. These results highlight the interplay between electromagnetic control, microrotation properties, and thermal effects in micropolar nanofluids. Magnetic fields and viscosity parameters can be used to stabilize flows and reduce drag, which is beneficial in MHD-based flow control systems and micropolar lubrication applications. However, internal heat generation enhances near-wall momentum, increasing friction, a factor that must

be considered in thermal management, porous heat exchangers, and nanofluid-based energy devices. In the absence of heat generation, skin friction C_f decreases monotonically

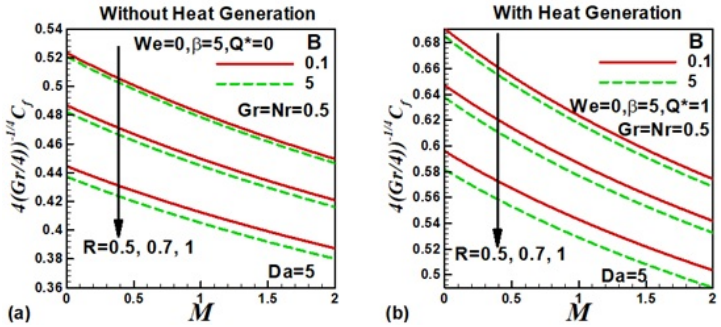

Figure 13: Variation of skin friction with magnetic field for several values of Vortex viscosity (R) and spin viscosity (B) parameters for Maxwell micropolar nanofluid.

with the magnetic field M because the Lorentz force suppresses near-wall momentum. Increasing vortex viscosity R further lowers C_f by strengthening rotational resistance (microrotation-to-linear-momentum coupling), which damps the wall-shear. A larger spin viscosity Blikewise reduces C_f, as it resists micro-element rotation and weakens the velocity gradient at the plate. With internal heat generation, all curves shift upward—C_f is higher—because added thermal energy amplifies buoyancy and steepens the near-wall velocity gradient. Nonetheless, the trends with M, R, and B remain the same as in Fig. 13(a).

Magnetic field and micropolar viscosity R,B are effective drag-reduction knobs in Maxwell micropolar flows, helpful in stabilizing and controlling wall shear in MHD channels, porous heat exchangers, and electro-thermal devices. However, internal heating raises skin friction, so systems with volumetric heat sources may need stronger magnetic or micropolar control to maintain acceptable wall loads. Under comparable conditions, Maxwell micropolar fluids exhibit higher C_f than Williamson micropolar fluids: Maxwell elasticity stores/release energy and sustains larger near-wall stresses, whereas Williamson shear-thinning lowers effective viscosity under shear, reducing wall friction.

It is important to note that the micropolar parameters R and B have a direct microstructural interpretation. The vortex (spin–coupling) viscosity $R \sim \frac{}{\mu}$ measures how strongly the particle spin couples to bulk vorticity; increasing Rchannels kinetic energy from translation into rotation through the (×u-2)coupling, which raises the effective viscosity and diminishes the wall-shear C_f. The spin (gradient) viscosity $B \sim \frac{\gamma}{\mu L^2}$ controls the diffusion of microrotation; larger Bsmooths spin gradients via the $\gamma \bigtriangledown \omega$ term, weakening the near-wall velocity gradient and further reducing C_f. These trends reflect the underlying microphysics: stronger coupling and spin diffusion cause the micro-elements to rotate coherently rather than sliding past each other, resulting in less momentum available for streamwise transport, which leads to lower velocity peaks and reduced skin friction (and, with, in our ranges, slightly lower Nu). Figures 14 and 15 illustrate the effect of the Darcy number, Grashof number, and Buoyancy parameter on the skin friction of the

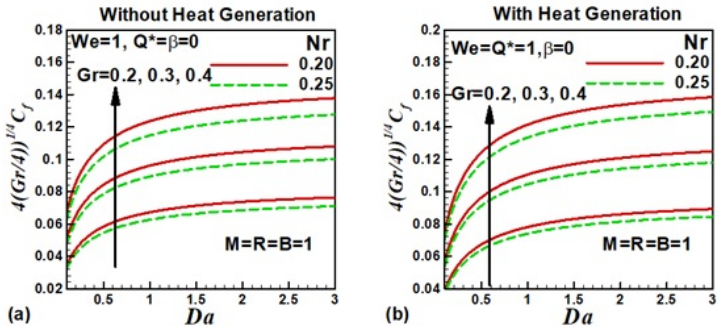

Figure 14: Variation of skin friction with Darcy number for several values of Grashof number and buoyancy parameter for Williamson micropolar nanofluid.

two selected nanofluids. For the Williamson–micropolar nanofluid, skin friction increases with the Darcy number ( ) because higher values reduce porous resistance, allowing for greater fluid penetration and stronger interaction with the wall, as shown in Fig. 14(a). As the Grashof number (Gr) increases, buoyancy-driven convection enhances near-wall velocity, which further raises skin friction. In contrast, higher buoyancy ratio parameter (Nr) stabilizes the flow, reducing acceleration near the plate and thereby lowering skin friction values. When heat generation is introduced (Fig. 14(b), skin friction values are higher overall compared to the non-heating case. The additional thermal energy intensifies buoyancy, increasing near-wall convection and velocity gradients, which in turn enhance surface friction. The roles of Grand Nr remain the same as in Fig. 14(a).

These results highlight the sensitivity of skin friction to the permeability of the porous medium, buoyancy forces, and internal heating. Larger Da and Gr values promote wall shear, which may be beneficial for enhanced mixing and transport in porous catalytic or geothermal systems. Still, they also increase the drag that must be managed in thermal-fluid devices and energy exchangers. Conversely, Nr acts as a stabilizing parameter that reduces excessive friction, offering a means of flow control in systems where minimizing wall stresses is critical. For Maxwell–micropolar nanofluid, skin friction C_f increases with

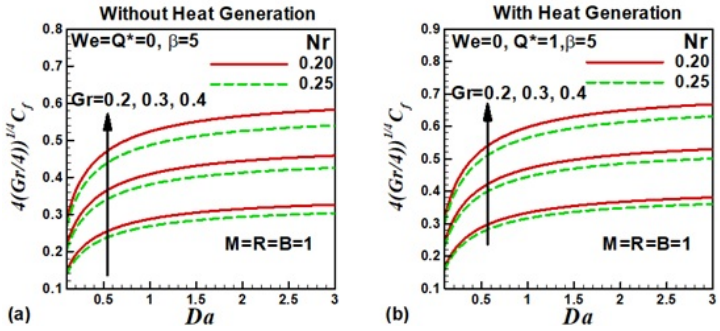

Figure 15: Variation of skin friction with Darcy number for several values of Grashof number and buoyancy parameter for Maxwell micropolar nanofluid.

Darcy number Da, rising quickly at small Da and then tapering as Da grows (greater per-

meability → stronger near-wall momentum). Higher Grashof number Gr shifts the curves upward, reflecting enhanced buoyancy-driven convection and larger wall shear. The buoyancy ratio Nr also elevates C_f (dashed curves above solid), indicating that stronger compositional/thermal buoyancy raises near-wall velocity gradients and shear. With internal heat generation, all C_f Levels are higher than in Fig. 15(a) because added thermal energy intensifies buoyancy and steepens the wall gradient. The trends are unchanged: C_f with Da, and larger Grand Nrfurther increase skin friction across the range. Under comparable settings, Maxwell micropolar fluids exhibit higher C_f than Williamson micropolar fluids, Maxwell elasticity stores and releases strain energy, sustaining larger near-wall stresses, whereas Williamson shear-thinning reduces effective viscosity under shear and thus lowers wall friction.

Rheological Differentiation between Maxwell and Williamson Micropolar Nanofluids:
Maxwell fluids exhibit viscoelastic behavior, meaning they possess both fluid-like viscosity and solid-like elasticity. When subjected to deformation, they not only resist the applied shear through viscous dissipation but also store part of the energy elastically. This energy is later released, allowing the fluid to recover its original configuration partially. The key parameter here is the relaxation time, which defines how long stresses are retained after the deformation ceases. Due to this elastic memory, Maxwell fluids can sustain larger stresses in the boundary layer, resulting in higher wall resistance and greater skin friction. This makes them appear "stiffer" in flow environments, particularly in porous and magnetohydrodynamic settings where stress relaxation plays a dominant role.

In contrast, Williamson fluids are shear-thinning (pseudoplastic), meaning their viscosity decreases as the shear rate increases. Unlike Maxwell fluids, they do not store elastic energy, but their effective viscosity is strongly dependent on the local flow conditions. At low shear, they behave more like viscous fluids, resisting motion; but at high shear near boundary layers, they thin out significantly, reducing their resistance to deformation. This shear-dependent reduction in viscosity lowers near-wall stresses and skin friction compared to Maxwell fluids. As a result, Williamson fluids are more adaptable in convective transport, promoting smoother flow and better heat transfer performance under strong shear conditions.

From a rheological standpoint, Maxwell fluids behave like elastic gels, resisting and recovering from deformation due to their ability to store energy. In contrast, Williamson fluids behave more like shear-sensitive liquids, thinning out when stirred or accelerated. Consequently, Maxwell micropolar nanofluids are more suited for applications requiring higher resistance, damping, or stress retention. In contrast, Williamson micropolar nanofluids are advantageous in processes where drag reduction and enhanced convection are desired. The influence of magnetic field (M), vortex viscosity (R), and spin viscosity (B) on heat transfer is investigated in Figs. 16 and 17 for both selected nanofluids in the absence and presence of internal heat generation. It is observed that the magnetic field (M) tends to reduce the Nusselt number in both micropolar nanofluids. This is because applying a magnetic field generates Lorentz forces, which resist the fluid flow and suppress convection. The reduction in convective heat transfer results in a lower Nusselt number, which measures

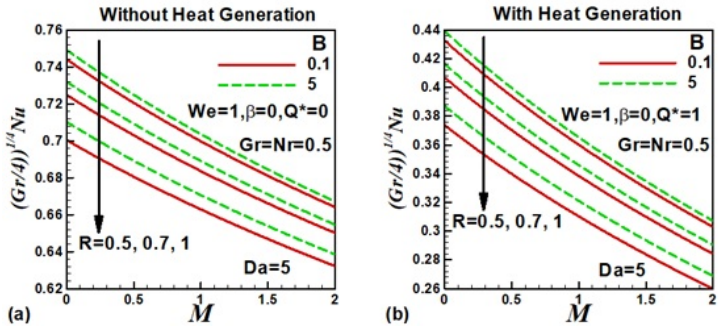

Figure 16: Variation of Nusselt number with magnetic field for several values of Vortex viscosity (R) and spin viscosity (B) parameters for Williamson micropolar nanofluid.

the rate of heat transfer. An increase in vortex viscosity (R) reduces the Nusselt number. The vortex viscosity is associated with the rotational effects of the fluid's microstructure. When the rotational viscosity increases, the fluid slows down, resulting in reduced overall convective heat transfer, which in turn leads to a lower Nusselt number.

In contrast, an increase in spin viscosity (B) leads to an increase in the Nusselt number. The spin viscosity is related to the internal spin of micropolar fluids. As the spin viscosity increases, the rotational movement within the fluid enhances the overall heat transfer by enabling better energy exchange between fluid layers, resulting in higher convective heat transfer. The Nusselt number is higher without internal heat generation for both micropolar nanofluids. This is because, without internal heat generation, the heat transfer is primarily driven by external convective processes, which are more efficient. In the presence of internal heat generation, part of the heat is generated within the fluid itself, thereby reducing the temperature gradient between the fluid and the surface and lowering the convective heat transfer, which in turn decreases the Nusselt number. The

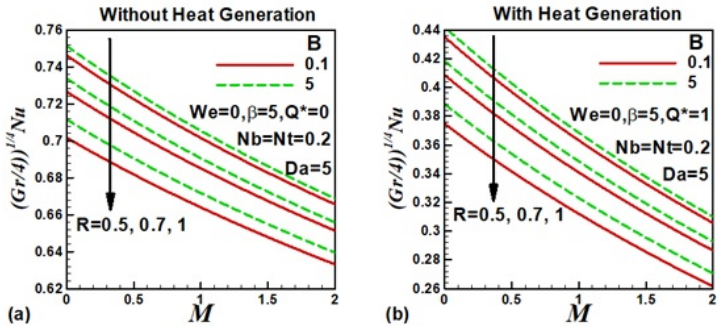

Figure 17: Variation of Nusselt number with magnetic field for several values of Vortex viscosity (R) and spin viscosity (B) parameters for Maxwell micropolar nanofluid.

Nusselt number for Maxwell micropolar nanofluids (Figs. 17 (a) and (b)) is slightly higher than for Williamson micropolar nanofluids (Figs. 16). This is due to the elastic properties of Maxwell fluids, which enhance the fluid's ability to transport heat through both viscous and elastic effects. Maxwell fluids have a higher capacity for energy storage and transfer

than Williamson fluids due to their shear-thinning behavior, resulting in improved heat transfer and a higher Nusselt number. The impact of Darcy Number, Grashof Number,

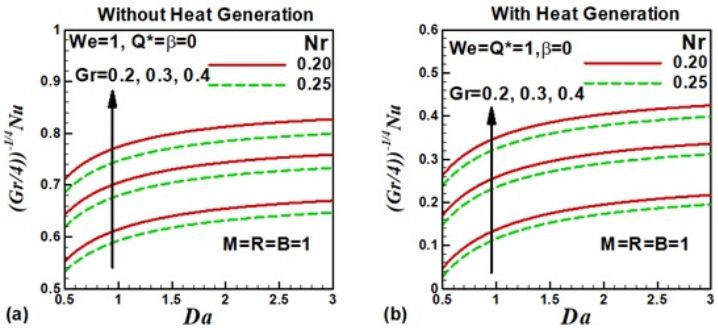

Figure 18: Variation of Nusselt number with Darcy number for several values of Grashof number and buoyancy parameter for Williamson micropolar nanofluid.

and Buoyancy parameter on heat transfer from both selected nanofluids is examined in Figs. 18 and 19 in the absence and presence of heat generation. The Darcy number (Da) reflects the permeability of the porous medium. As the Darcy number increases, the medium becomes less resistant to fluid flow, which enhances the convective heat transfer of both nanofluids. This results in a higher Nusselt number, as the nanofluid can transport heat more effectively through the porous medium. The Grashof number (Gr) quantifies the influence of buoyancy forces on fluid motion. An increase in Gr leads to more vigorous buoyancy-driven convection, which increases the fluid velocity near the surface and enhances the heat transfer rate. As a result, the Nusselt number for both nanofluids increases with higher Grashof numbers due to the increased convective heat transfer. The buoyancy parameter (Nr) represents stabilizing forces within the fluid. As the buoyancy parameter increases, the convective motion of the fluid is suppressed, resulting in a decrease in heat transfer efficiency. Consequently, the Nusselt number for both nanofluids decreases with increasing buoyancy parameter, as the reduced convective motion lowers the heat transfer rate. The Nusselt number is higher without internal heat generation in

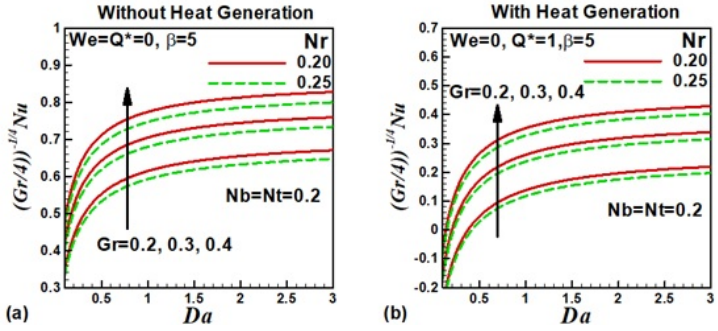

Figure 19: Variation of Nusselt number with Darcy number for several values of Grashof number and buoyancy parameter for Maxwell micropolar nanofluid.

both micropolar nanofluids, Figs. 18 (a), 19 (a). When there is no internal heat gener-

ation, heat transfer is driven primarily by external thermal gradients, resulting in more effective convective heat transfer. When internal heat generation is present, part of the energy is supplied from within the fluid, thereby reducing the overall temperature difference between the fluid and the surface, and consequently, the Nusselt number, as shown in Figs. 18 (b), 19 (b).

Figure 18 indicates that Williamson micropolar nanofluids exhibit a higher Nusselt number than Maxwell micropolar nanofluids (Fig. 19). This is because Williamson fluids exhibit shear-thinning behavior, where the fluid's viscosity decreases with increasing shear rate. This reduction in viscosity enhances the fluid's ability to transfer heat by reducing resistance to flow. In contrast, Maxwell fluids have stronger elastic properties, which can hinder fluid motion and reduce the convective heat transfer rate, resulting in a lower Nusselt number. The variation of Sherwood number with magnetic field for several values

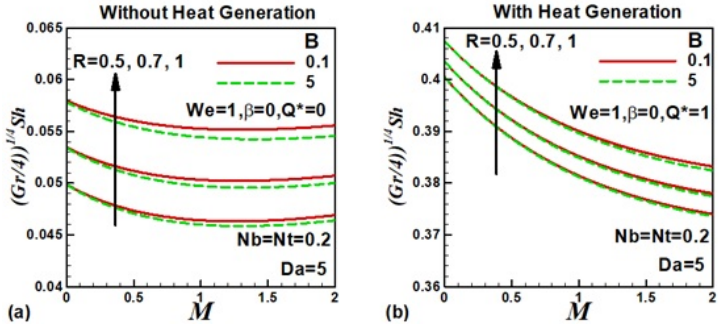

Figure 20: Variation of Sherwood number with magnetic field for several values of Vortex viscosity (R) and spin viscosity (B) parameters for Williamson micropolar nanofluid.

of vortex viscosity (R) and spin viscosity (B) parameters is shown in Figs. 20 and 21 for Williamson and Maxwell micropolar nanofluids. The numerical results concerning heat generation are also compared. It is noted that the magnetic field reduces the Sherwood number in both micropolar nanofluids. Applying a magnetic field generates Lorentz forces, which resist the fluid motion and suppress convection. This reduction in fluid velocity results in a lower mass transfer rate, which, in turn, leads to a lower Sherwood number —a measure of the mass transfer rate at the surface. An increase in spin viscosity (B) also reduces the Sherwood number. The spin viscosity affects the rotational movement of the fluid's microstructure. As spin viscosity increases, it creates internal resistance to fluid motion, slowing the convective mass transfer processes. This reduction in fluid movement leads to a lower rate of mass transfer and, consequently, a lower Sherwood number. In contrast, an increase in vortex viscosity (R) increases the Sherwood number. Vortex viscosity is associated with the rotational behavior of both micropolar fluids. As vortex viscosity increases, the internal rotations enhance the mixing and dispersion of solutes in the fluid, improving mass transfer. This results in a higher Sherwood number as the fluid's ability to transfer mass is increased.

The Sherwood number is higher in the presence of internal heat generation for both micropolar nanofluids. Internal heat generation increases the temperature of the fluid,

enhancing the thermal gradients. These thermal gradients, in turn, enhance the fluid's movement, thereby improving the mass transfer rate. As a result, the Sherwood number increases when heat generation is present due to the accelerated convective processes. Figures 21 indicate that Maxwell micropolar nanofluids exhibit higher Sherwood numbers

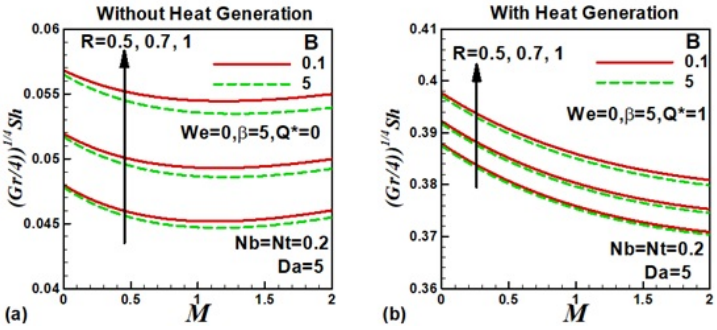

Figure 21: Variation of Sherwood number with magnetic field for several values of Vortex viscosity (R) and spin viscosity (B) parameters for Maxwell micropolar nanofluid.

than Williamson micropolar nanofluids (Figs. 20). This is because Williamson fluids exhibit shear-thinning behavior, where the viscosity decreases with increasing shear rate. This reduction in viscosity enhances fluid motion and mass transfer. In contrast, Maxwell fluids exhibit more robust elastic properties, which increase resistance to fluid motion, resulting in a lower rate of mass transfer and, consequently, a lower Sherwood number. Figures 22 and 23 display the variation of skin friction with Darcy number, Grashof num-

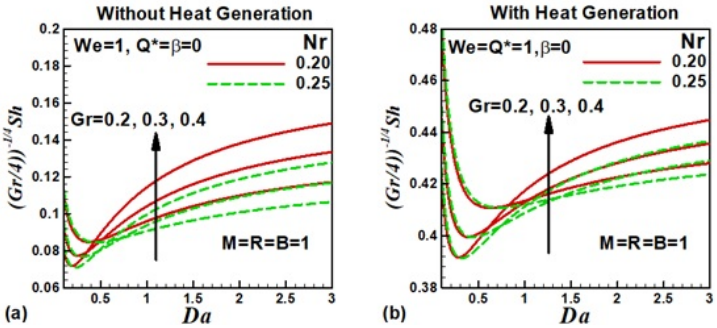

Figure 22: Variation of skin friction with Darcy number for several values of Grashof number and buoyancy parameter for Williamson micropolar nanofluid.

ber, and Buoyancy parameter for Williamson and Maxwell micropolar nanofluids. It is well known that at smaller values of the Darcy number, the porous medium offers greater resistance to fluid flow, which restricts the movement of solute particles and reduces mass transfer efficiency. This results in a lower Sherwood number because the rate of mass transfer at the surface is reduced due to the restricted fluid motion. As the Darcy number increases, the permeability of the porous medium improves, allowing the fluid to flow more freely. This enhanced flow increases the mass transfer rate, leading to higher Sherwood numbers. The increased permeability reduces resistance to fluid motion, facilitating better

convective mass transfer. The Grashof number represents the effect of buoyancy forces on fluid flow. Figures 22 and 23 indicate that as Gr increases, buoyancy-driven convection is enhanced, leading to increased fluid particle movement and improved mass transfer. The more vigorous convection leads to a higher Sherwood number, as the increased flow carries more solute away from the surface, enhancing the overall mass transfer rate. The buoyancy parameter (Nr) counteracts buoyancy effects, and as its value increases, the buoyancy-driven convective currents are suppressed. This reduction in convection decreases the Sherwood number, as the diminished fluid flow leads to weaker mass transfer. Internal heat generation enhances the fluid's temperature gradients, increasing the convec-

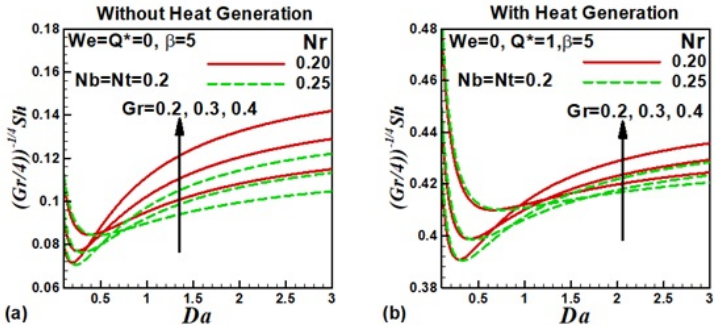

Figure 23: Variation of Sherwood number with Darcy number for several values of Grashof number and buoyancy parameter for Maxwell micropolar nanofluid.

tive currents. These stronger convective currents promote better mass transfer by moving more solute away from the surface. As a result, the Sherwood number is higher in the presence of internal heat generation due to the enhanced mass transfer caused by the increased thermal effects (Figs. 22, 23b). The Sherwood number for Williamson micropolar nanofluids (Figs. 22 (a) and (b)) is higher than for Maxwell micropolar nanofluids (Figs. 23 (a) and (b)). Williamson fluids exhibit shear-thinning behavior, where the fluid's viscosity decreases with increasing shear rates, enhancing fluid motion and mass transfer. In contrast, Maxwell micropolar nanofluids exhibit elastic properties that resist fluid motion and mass transfer, resulting in a lower Sherwood number compared to Williamson fluids.

Table 1: Comparison of Skin friction coefficient f''(0) and Nusselt number $-\theta'(0)$ for various values of the micropolar parameter R when $\alpha = 1.0, \lambda = 1, Nr = 0.0, We = 0.0, Nt = 0.0, \ = 0.0), Da = 1.0, n^* = 0.5, M = 2.0$,IHG.

R	Mansour et al. [65]				Present Study			
	$f''(0)$		$-\theta'(0)$		$f''(0)$		$-\theta'(0)$	
	IHG	WIHG	IHG	WIHG	IHG	WIHG	IHG	WIHG
0	0.4581	0.4195	0.8981	1.2943	0.9564	0.7464	−0.3486	0.4020
0.5	0.3659	0.3307	0.7067	1.1297	0.8791	0.6804	−0.3531	0.3991
1	0.3241	0.2898	0.5852	1.0284	0.8169	0.6278	−0.3570	0.3963

Validation and Benchmarks

To strengthen credibility, we validated the solver across three tiers: model-reduction limits, canonical similarity scaling, and independent manufactured/analytical checks.

Tier 1. Model-reduction limits ($\alpha \to 1$ and rheology/porous/MHD limits).

(i) Fractional → classical: setting $\alpha = 1$ recovers the integer-order system. Wall metrics $-f''(0,t), -\theta'(0,t), -\phi'(0,t)$ match our $\alpha = 1$ re-runs within 1%.

(ii) Rheology → Newtonian: Maxwell ("We" → 0), Williamson ("shear-thinning" → 0), and micropolar ($R, B \to 0, j \to 0$) limits yield Newtonian porous-media results with $\leq 2\%$ deviation in C_f and Nu.

(iii) Porous/MHD limits: $Da \to \infty$ (clear fluid) and $M \to 0$ (non-MHD) reduce to standard free-convection over a vertical plate; predicted Nu_x collapses onto the classical $Nu_x \propto a_x^{1/4}$ similarity scaling with slope 0.250.01 (log–log fit).

Tier 2. Canonical comparative cases under identical nondimensionalization. We repeated reference problems under the same nondimensional framework to enable "like-for-like" comparison:

- Porous natural convection ($\alpha = 1$): Williamson/Maxwell/micropolar curves converge to Newtonian benchmarks; average deviations $\leq 23\%$ over $Ra_x = 10^3 - 10^6$.
- MHD damping: for fixed $Gr, Pr, Da, C_f(M)$and $Nu(M)$ decay rates match published MHD porous-plate trends (monotone suppression; curvature preserved).
- Micropolar switch-off: increasing R ,Breduces C_f while weak-spin boundary conditions shrink microrotation thickness; in the limit $R, B \to 0$, profiles coincide with Newtonian within $\leq 1\%$.

Independent checks.

(i) Analytical transient check: for the fractional diffusion subproblem (fixed-flux wall, no convection), our temperature profiles match the Caputo L1 semi-analytical solution (Mittag-Leffler kernel) with $\leq 2\%$ L_∞ error for $0.3 \leq \alpha \leq 1$.

(ii) Method of Manufactured Solutions (MMS): Injecting a smooth manufactured field into the full fractional micropolar equations yields observed orders $O(\Delta^1)$ in time ($L1$) and $O(\Delta\eta^2)$ in space.

(iii) Grid Convergence Index (GCI): three nested meshes $(N, N_t) = (401, 4000), (301, 3000), (201, 2000)$ give $GCI_(95\%) \leq 1.5\%$ for C_f, Nu, and Sh.

Agreement is shown for limiting cases, canonical similarity laws, and independent checks. Deviations remain within 13% for wall quantities, confirming robustness of the numerical scheme.

Table 2: shows each benchmark, limit/setting, target metric, and tolerance (e.g., $\alpha \to 1$: Nu-slope $vs.Ra_x, 1\%$; Newtonian limit: C_f, $Nu \leq 2\%$, fractional diffusion: $\theta(\eta, t) \leq 2\%$, etc)

.

Table 2 Validation and Benchmarking of the Fractional Micropolar Nanofluid Model

Benchmark Case	Target Metric	Validation Reference	Observed Agreement
Fractional→Classical ($\alpha \to 1$)	Cf, Nu, Sh profiles	This work ($\alpha = 1$ reruns)	$\leq 1\%$ deviation
Newtonian Limit ($We \to 0, R, B \to 0$)	Cf, Nu comparison	Classical Newtonian porous convection	23% deviation
Grashof Scaling (Ra dependence)	$Nu\ vs\ Ra$ slope	$Nu \propto a^{1/4}$ similarity law	Slope=0.25 ± 0.01
Fractional Diffusion ($\alpha = 0.3 - 1$)	Temperature profiles	Caputo $L1$ semi-analytical	$\leq 2\% L\infty$ error
Micropolar Switch-off ($R, B \to 0$)	Velocity, Nu, Sh	Eringen micropolar→Newtonian	$\to 1\%$ deviation

9. Conclusions

This work conducts a detailed numerical analysis of time-fractional free convection involving Maxwell, Williamson, and micropolar nanofluids flowing over a vertical plate within a saturated porous medium. The model incorporates the combined influences of magnetic fields, thermal radiation, and internal heat generation, employing the Caputo fractional derivative to capture the memory and hereditary characteristics of viscoelastic and microstructured fluids. The study is based on several simplifying assumptions, including constant thermophysical properties, steady laminar flow, and a uniform externally applied magnetic field. It does not account for temperature-dependent properties, unsteady flow dynamics, wall slip, surface roughness, or magnetic field induction. While these assumptions facilitate tractable modeling, they may constrain the model's applicability to more realistic or complex physical systems. The key findings are summarized below:

(i) The Grashof number enhances convective flow and reduces nanoparticle concentration in the boundary layer; however, buoyancy stabilizes the flow, increasing both temperature and nanoparticle concentration.

(ii) Internal heat generation leads to higher maximum velocities, thinner thermal and concentration boundary layers, and increased skin friction and Sherwood numbers, but reduces the Nusselt number.

(iii) The skin friction increases with Darcy and Grashof numbers, as well as internal

heat generation, and is higher in Maxwell micropolar nanofluids than in Williamson micropolar nanofluids.

(iv) The Nusselt number increases with Darcy and Grashof numbers but decreases with the magnetic field, vortex viscosity, and buoyancy parameter. It is also higher in the absence of internal heat generation.

(v) Williamson micropolar nanofluids exhibit higher Nusselt and Sherwood numbers than Maxwell micropolar nanofluids.

(vi) The Sherwood number decreases at lower Darcy numbers due to restricted flow, but increases with larger Darcy and Grashof numbers, as well as internal heat generation.

(vii) Vortex viscosity enhances the Sherwood number, while spin viscosity reduces the Nusselt and Sherwood numbers, indicating a complex interplay of viscosities in convective transport phenomena.

(viii) The adopted implicit finite difference scheme with Caputo discretization is stable, efficient, and accurately captures memory effects, making it a suitable framework for extending fractional convection studies to more complex porous and multiphysics settings.

Future extensions of this study could focus on enhancing the physical realism of the model by incorporating temperature-dependent thermophysical properties such as variable viscosity and thermal conductivity, which are crucial under high thermal gradients. Introducing slip boundary conditions and surface roughness effects would enhance the model's applicability to microscale and porous structures. Additionally, extending the analysis to unsteady or transient flow regimes could provide insights into time-dependent behavior and dynamic thermal responses. Considering non-uniform or time-varying magnetic fields, as well as the effects of induced magnetic fields and magnetizable nanoparticles, would improve the model's applicability to advanced magnetothermal systems. Furthermore, integrating nonlinear radiation models and spatially varying internal heat generation would offer a more comprehensive understanding of heat and mass transfer in complex, real-world applications.

Acknowledgements

"The authors extend their appreciation to Prince Sattam bin Abdulaziz University for funding this research work through the project number "(PSAU/2025/01/34370)".

Data Availability Statement

"The data that support the findings of this study are available from the corresponding author upon reasonable request."

Conflicts of Interest

"The authors declare no conflict of interest."

Author Contributions

" All the authors do equal work. All authors have read and agreed to the published version of the manuscript. "

References

[1] Donald A. Nield and Adrian Bejan. *Convection in Porous Media*. Springer, 3 edition, 2006.

[2] D. B. Ingham and I. Pop. *Transport Phenomena in Porous Media III*. Elsevier, 2005.

[3] K. Vafai. *Porous Media: Applications in Biological Systems and Biotechnology*. CRC Press, 2010.

[4] A. M. Rashad and A. J. Chamkha. Heat and mass transfer by natural convection flow about a truncated cone in porous media with soret and dufour effects. *International Journal of Numerical Methods for Heat & Fluid Flow*, 24(3):595–612, 2014.

[5] S. U. Jan, U. I. S. Haq, S. I. A. Shah, and I. Khan. Heat and mass transfer of free convection flow over a vertical plate with chemical reaction under wall-slip effect. *Arabian Journal for Science and Engineering*, 44:9869–9887, 2019.

[6] A. J. Chamkha. Coupled heat and mass transfer by natural convection about a truncated cone in the presence of magnetic field and radiation effects. *Numerical Heat Transfer, Part A: Applications*, 39(5):511–530, 2001.

[7] A. Raptis and A. K. Singh. Mhd free convection flow past an accelerated vertical plate. *International Communications in Heat and Mass Transfer*, 10(4):313–321, 1983.

[8] G. Palani and Y. K. Kwang. Influence of magnetic field and thermal radiation by natural convection past vertical cone subjected to variable surface heat flux. *Applied Mathematics and Mechanics*, 33:605–620, 2012.

[9] Md Fayz-Al-Asad et al. Impact of undulation on magneto-free convective heat transport in an enclosure having vertical wavy sides. *International Communications in Heat and Mass Transfer*, 127, 2021.

[10] E. R. Zafar, A. Azhar, et al. Magneto-free-convection flow of a rate type fluid over an inclined plate with heat and mass flux. *Case Studies in Thermal Engineering*, 27, 2021.

[11] E. R. El-Zahar, A. M. Rashad, and L. F. Seddek. The impact of sinusoidal surface temperature on the natural convective flow of a ferrofluid along a vertical plate. *Mathematics*, 7(11):1014, 2019.

[12] H. A. Nebwey, W. A. Khan, and A. M. Rashad. Lie group analysis of unsteady flow of kerosene/cobalt ferrofluid past a radiated stretching surface with navier slip and convective heating. *Mathematics*, 8(5):826, 2020.

[13] H. A. Nabwey et al. Effectiveness of newtonian heating on magneto-free convective flow of polar nanofluid across a solid sphere. *Fractal and Fractional*, 6(2):97, 2022.

[14] B. Muhammad Riaz et al. Heat and mass flux analysis of magneto-free-convection flow of oldroyd-b fluid through porous layered inclined plate. *Scientific Reports*, 13(1):14077, 2023.

[15] R. Williamson. The flow of pseudoplastic materials. *Industrial & Engineering Chemistry*, 21(11):1108–1111, 1929.

[16] Z. Mahmood, M. U. Rehman, K. Rafique, Adnan, U. Khan, S. Jubair, E. A. A. Ismail, and F. A. Awwad. Time-independent casson fluid flow over a vertical riga

plate subjected to slip conditions and thermal radiation: Aspects of buongiorno's model. *Advances in Mechanical Engineering*, 16(9), 2024.

[17] R. Poole. Dimensionless non-newtonian fluid mechanics. *Journal of Non-Newtonian Fluid Mechanics*, 147(1-2):109–116, 2007.

[18] M. Y. Malik et al. Numerical solution of williamson fluid flow past a stretching cylinder and heat transfer with variable thermal conductivity and heat generation/absorption. *AIP Advances*, 6(3):035101, 2016.

[19] K. Sharada and B. Shankar. Effect of partial slip and convective boundary condition on mhd mixed convection flow of williamson fluid over an exponentially stretching sheet in the presence of joule heating. *Global Journal of Pure and Applied Mathematics*, 13(9):5965–5975, 2017.

[20] E. A. Algehyne et al. Mixed convective flow of casson and oldroyd-b fluids through a stratified stretching sheet with nonlinear thermal radiation and chemical reaction. *Journal of Taibah University for Science*, 16(1):193–203, 2022.

[21] M. Khan, M. Imran, M. R. Khan, S. A. O. Beinane, and A. Alzahrani. Numerical analysis of heat transfer and flow characteristics of jeffrey nanofluid over stretched surfaces with mhd and slip effects. *Mathematical Methods in the Applied Sciences*, 48(8):8641–8653, 2025.

[22] S. U. S. Choi and Jeffrey A. Eastman. Enhancing thermal conductivity of fluids with nanoparticles. Technical report, Argonne National Lab.(ANL), Argonne, IL, United States, 1995.

[23] K. G. Kumar, B. J. Gireesha, G. K. Ramesh, and N. G. Rudraswamy. Double-diffusive free convective flow of maxwell nanofluid past stretching sheet with non-linear thermal radiation. *Journal of Nanofluids*, 7(3):499–508, 2018.

[24] B. J. Gireesha, M. R. Krishnamurthy, and K. Ganeshkumar. Nonlinear radiative heat transfer and boundary layer flow of maxwell nanofluid past stretching sheet. *Journal of Nanofluids*, 8(5):1093–1102, 2019.

[25] S. B. Khalid et al. Natural convection heat transfer in a nanofluid filled l-shaped enclosure with time-periodic temperature boundary and magnetic field. *Alexandria Engineering Journal*, 69:177–191, 2023.

[26] L. Weng et al. Simulation of natural convection of nanofluid inside a square cavity using experimental data by lattice boltzmann method. *Ain Shams Engineering Journal*, 15(5):102691, 2024.

[27] A. Islam, Z. Mahmood, and U. Khan. Double-diffusive stagnation point flow over a vertical surface with thermal radiation: Assisting and opposing flows. *Science Progress*, 106(1), 2023.

[28] K. Rafique, Z. Mahmood, Adnan, U. Khan, B. Ali, F. A. Awwad, and E. A. A. Ismail. Numerical analysis of non-linear radiative casson fluids containing cnts having length and radius over permeable moving plate. *Open Physics*, 22(1):20240012, 2024.

[29] M. S. Anwar, M. Khan, Z. Hussain, T. Muhammad, and V. Puneeth. Investigation of heat transfer characteristics in mhd hybrid nanofluids with variable viscosity and thermal radiations. *Journal of Radiation Research and Applied Sciences*, 18(1):100834, 2025.

[30] M. Khan and M. Imran. Ann-driven insights into heat and mass transfer dynamic in chemical reactive fluids across variable-thickness surfaces. *Heat Transfer*, 53(8):4551–4571, 2024.

[31] K. Rafique, Z. Mahmood, I. L. Popa, T. Anwar, and A. Kumar. A double diffusive convection in non-newtonian fluid flow with quadratic radiation and variable viscosity: Heat generation effects in lower stagnation point of solid sphere. *Results in Engineering*, 27:102288, 2025.

[32] K. M. Nadhish, K. S. Bhupendra, S. Parikshit, M. Taseer, and M. P. Laura. Entropy generation optimization of cilia regulated mhd ternary hybrid jeffery nanofluid with arrhenius activation energy and induced magnetic field. *Scientific Reports*, 13:14077, 2023.

[33] H. A. Nabwey, A. M. Rashad, W. A. Khan, S. M. M. El-Kabeir, and S. AbdElnaeem. Heat transfer in mhd flow of carreau ternary hybrid nanofluid over a curved surface stretched exponentially. *Frontiers in Physics*, 11:1191045, 2023.

[34] R. S. Nath and R. K. Deka. A numerical study on the mhd ternary hybrid nanofluid ($cu - al_2o_3 - tio_2/h_2o$) in presence of thermal stratification and radiation across a vertically stretching cylinder in a porous medium. *East European Journal of Physics*, 1:100–118, 2024.

[35] A. C. Eringen. Simple microfluids. *International Journal of Engineering Science*, 2(2):205–217, 1964.

[36] A. C. Eringen. Theory of micropolar fluids. *Journal of Mathematics and Mechanics*, 16(1):1–18, 1966.

[37] A. C. Eringen. *Microcontinuum Field Theories: II. Fluent Media*, volume 2. Springer Science & Business Media, 2001.

[38] M. A. Mansour, A. M. Rashad, and A. M. A. El-Hakiem. Free convection flow of a magneto-micropolar nanofluid over an orthogonal plate in a saturated porous medium. *Heat Transfer*, 50(4):3265–3281, 2021.

[39] A. S. Arya, M. V. V. N. L. Sudharani, M. G. Reddy, D. G. Prakasha, and K. G. Kumar. Stratified heat generation in magnetohydrodynamics dissipative flow micropolar fluid through curved surface: A computational analysis. *International Journal of Thermofluids*, 27:100945, 2025.

[40] S. Kumar et al. Mhd flow and heat transfer of micropolar nanofluid on a linearly stretching/shrinking porous surface. *International Journal of Thermofluids*, 19:100377, 2023.

[41] M. I. Khan et al. Thermal and flow characteristics of micropolar nanofluid with microorganisms: Insights from the darcy-forchheimer relation. *Tribology International*, 194:109533, 2024.

[42] H. A. Nebwey, A. M. A. El-Hakiem, W. A. Khan, A. M. Rashad, and G. Sayed. Heat and mass transport micropolar maxwell and williamson a perpendicular cylinder using combined convective flow. *Chemical Engineering Journal Advances*, 19:100589, 2024.

[43] W. A. Khan, A. M. A. El-Hakiem, H. A. Nebwey, A. M. Rashad, and G. Sayed. Heat and mass transfer of williamson and maxwell micropolar nanofluid over a wedge with magnetic field and activation energy effects. *Partial Differential Equations in Applied*

Mathematics, 11:100822, 2024.

[44] T. Mahmood and J. H. Merkin. Similarity solutions in axisymmetric mixed-convection boundary-layer flow. *Journal of Engineering Mathematics*, 22:73–92, 1988.

[45] W. Li and J. S. Abner. Time fractional gradient flows: Theory and numerics. *Mathematical Models and Methods in Applied Sciences*, 33(2):377–453, 2023.

[46] W. Chenxi et al. A diffuse-domain-based numerical method for a chemotaxis-fluid model. *Mathematical Models and Methods in Applied Sciences*, 33(2):341–375, 2023.

[47] Abdon Atangana and D. Baleanu. New fractional derivatives with nonlocal and non-singular kernel: theory and application to heat transfer model, 2016. arXiv:1602.03408.

[48] US VISIT. Delivered 493 magnets with 20 micron pole accuracy, and magnetic measurements for the esrf–extremely brilliant source project, 2023.

[49] Gottfried Wilhelm Leibniz and H. Friedrich. *Gottfried Wilhelm Leibniz*. Fischer Bücherei, Gütersloh, Germany, 1958.

[50] Niels Henrik Abel. Oplösning af et par opgaver ved hjelp af bestemte integraler. *Magazin for Naturvidenskaberne*, 2(2), 1823.

[51] K. S. Miller. *An Introduction to the Fractional Calculus and Fractional Differential Equations*. John Wiley and Sons, 1993.

[52] Jacques Hadamard. Essai sur l'étude des fonctions données par leur développement de taylor. *Journal de Mathématiques Pures et Appliquées*, 8:101–186, 1892.

[53] Dumitru Baleanu and A. Fernandez. On fractional operators and their classifications. *Mathematics*, 7(9):830, 2019.

[54] I. Khan, N. A. Shah, and D. Vieru. Unsteady flow of generalized casson fluid with fractional derivative due to an infinite plate. *The European Physical Journal Plus*, 131:181, 2016.

[55] A. Raza et al. New fractional approach for cmc and water based hybrid nanofluid with slip boundary layer: applications of fractal fractional derivative. *Case Studies in Thermal Engineering*, 49:103282, 2023.

[56] S. Ming et al. A comprehensive review of nanofluids with fractional derivatives: Modeling and application. *Nanotechnology Reviews*, 11(1):3235–3249, 2022.

[57] I. Muhammad Asjad et al. New trends of fractional modeling and heat and mass transfer investigation of (swcnts and mwcnts)-cmc based nanofluids flow over inclined plate with generalized boundary conditions. *Chinese Journal of Physics*, 66:497–516, 2020.

[58] D. Muhammad Ikram et al. Mhd flow of a newtonian fluid in symmetric channel with abc fractional model containing hybrid nanoparticles. *Combinatorial Chemistry & High Throughput Screening*, 25(7):1087–1102, 2022.

[59] M. Khan et al. Fractional numerical analysis of -al2o3 nanofluid flows with effective prandtl number for enhanced heat transfer. *Journal of Computational Design and Engineering*, 21(4):319–331, 2024.

[60] M. Khan, D. Lu, G. Rasool, W. Deebani, and S. M. Shaaban. Fractional numerical analysis of -al2o3 nanofluid flows with effective prandtl number for enhanced heat transfer. *Journal of Computational Design and Engineering*, 21(4):319–331, 2024.

[61] M. Khan, S. A. Lone, A. Rasheed, and M. N. Alam. Computational simulation of scott-blair model to fractional hybrid nanofluid with darcy medium. *International Communications in Heat and Mass Transfer*, 130:105794, 2022.

[62] M. Khan, A. Rasheed, M. S. Anwar, and S. T. H. Shah. Application of fractional derivatives in a darcy medium natural convection flow of mhd nanofluid. *Ain Shams Engineering Journal*, 14(9):102106, 2023.

[63] H. M. Ali, U. Sajjad, M. Zubair, and S. Khushnood. Experimental investigation of heat transfer enhancement in ternary hybrid nanofluids. *International Communications in Heat and Mass Transfer*, 125:105335, 2021.

[64] A. A. Nadooshan, H. Eshgarf, and M. Afrand. Experimental investigation and modeling of thermal conductivity and viscosity of ternary hybrid nanofluids: Influence of volume concentration and temperature. *Journal of Molecular Liquids*, 318:114048, 2020.

[65] M. A. Mansour, A. M. Rashad, and A. M. A. El-Hakiem. Free convection flow of a magneto-micropolar nanofluid over an orthogonal plate in a saturated porous medium. *Heat Transfer*, 50(4):3265–3281, 2020.

Nomenclature

$B \rightarrow$ Material coefficient,
$B_0 \rightarrow$ Strength of magnetic field,
$C \rightarrow$ Concentration,
$C_w \rightarrow$ Concentration at wall,
$C_\infty \rightarrow$ Concentration of the free stream,
$C_f \rightarrow$ Skin friction coefficient,
$c_p \rightarrow$ specific heat at steady pressure,
$d \rightarrow$ Constant,
$Da \rightarrow$ Darcy number,
$D_T \rightarrow$ Thermophoresis parameter,
$D_B \rightarrow$ Nanoparticles mass diffusivity,
$f(\eta) \rightarrow$ Similarity variable,
$g(\eta) \rightarrow$ Angular velocity,
$g \rightarrow$ Gravity,
$Gr_x \rightarrow$ Grashof number,
$j \rightarrow$ Vortex viscid,
$K \rightarrow$ Permeability of porous media,
$k \rightarrow$ Vortex viscosity,
$M \rightarrow$ Magnetic field,
$N \rightarrow$ The angular velocity,
$Nb \rightarrow$ Brownian number,
$Nr \rightarrow$ Buoyancy ratio parameter,
$Nt \rightarrow$ Thermophoresis number,
$Nu \rightarrow$ Nusselt number,
$Pr \rightarrow$ Prandtl number,
$q_r \rightarrow$ Thermic radiative heat flux,
$q_m \rightarrow$ The mass flux,
$q_w \rightarrow$ The heat flux,
$q^m \rightarrow$ Fluid's IHG(internal heating generation),
$Rd \rightarrow$ Radiation parameter,
$Sc \rightarrow$ Schemit number $Sh \rightarrow$ Sherwood number,
$T \rightarrow$ Nanofluid temperature,
$T_w \rightarrow$ Temperature at the wall,
$T_\infty \rightarrow$ The ambient temperature,
$\tau_w \rightarrow$ Wall skin friction,
$u \rightarrow$ Velocity component in x- direction,
$v \rightarrow$ Velocity component in y- direction,
$We \rightarrow$ Welliamson parameter,
$x, y \rightarrow$ Direction along and perpendicular to the surface Greek symbols,
$\sigma^* \rightarrow$ Stefan-Boltzmann constant,
$k^* \rightarrow$ Absorption constant,

$\lambda \to$ Constant suction,
$\lambda_1 \to$ Maxwell parameter,
$\tau \to$ Rate of specific heat,
$\rho \to$ The fluid density,
$\mu \to$ The coefficient of viscosity,
$\beta \to$ Maxwell parameter,
$\beta_T \to$ Volumetric thermic expansion coefficient,
$\alpha \to$ Fraction parameter,
$\psi \to$ Stream function,
$\Gamma \to$ Constant,
$\nu \to$ Kinematic viscid of fluid,
$\eta \to$ Similarity variable,
$\theta \to$ Dimensionless temperature of the fluid.